Influence of Electromagnetic Stirring on the Amount of Equiaxed Solidification during Continuous Casting

Diploma Thesis

submitted by

Sebastian Michelic
Chair of Metallurgy
Montanuniversität Leoben

Leoben, December 2006

Diploma Thesis

S 645

The Chair of Metallurgy poses
the following diploma thesis topic
to **Sebastian Michelic**:

Influence of Electromagnetic Stirring on the Amount of Equiaxed Solidification during Continuous Casting

During continuous casting of high carbon steels, the maximisation of the amount of equiaxed solidification is a declared aim, in order to positively influence the formation of centre segregations. Next to the superheat, electromagnetic stirring has proven most effective in previous observations. All gathered results should be combined into a model for the equiaxed solidification and implemented into a thermal model within the frame of a joint research project between voestalpine Stahl Donawitz GmbH & Co. KG and the „Christian-Doppler Laboratory for Metallurgical Fundamentals of Continuous Casting Processes“.

Tasks:

- **Study of the literature concerning EMS, especially focusing on the influences of EMS on the columnar to equiaxed transition.**
- **Modification of the existing thermal model for an incorporation of EMS**
- **Realisation of the fragmentation of dendrites under consideration of the superheat and the velocity at the dendrite tips.**
- **Implementation of the CET model into the thermal model**
- **Evaluation and illustration of the results for various casting parameters**
- **Validation of the results with practical plant trials**

Leoben, May 2006 Univ.Prof. DI Dr.mont. Wilfried Krieger

Einfluss des elektromagnetischen Rührens auf den Anteil ungerichteter Erstarrung beim Stranggießen von Stahl

Diplomarbeit
eingereicht von

Sebastian Michelic

Kurzfassung

Während des Vergießens von hochkohligen Stählen führt die Ausbildung von Makroseigerungen zu Qualitätseinbußen beim Gussprodukt. Zur Minimierung hat sich ein möglichst großer Anteil an ungerichteter Erstarrung als günstig erwiesen, welcher einerseits durch eine geringe Überhitzung und andererseits durch elektromagnetisches Rühren in der Kokille erreicht werden kann.

In der vorliegenden Arbeit werden Ansätze aus der Literatur zur Modellierung der Ausbildung der ungerichteten Erstarrung untersucht. Dabei werden sowohl die Mechanismen der Dendriten-fragmentierung aufgrund des elektromagnetischen Rührens als auch die heterogene Keimbildung berücksichtigt. Auf Basis dieser Ansätze, wird ein Modell für die Prognose des Anteils der ungerichteten Erstarrung in ein bestehendes Erstarrungsmodell implementiert. Anhand von parallel durchgeführten Betriebs-versuchen an einer Stranggießanlage, werden so erste Abschätzungen über die Aussagekraft eines solchen Modells getroffen.

Influence of Electromagnetic Stirring on the Amount of Equiaxed Solidification during Continuous Casting

Diploma Thesis
submitted by

Sebastian Michelic

Abstract

The formation of macro segregations during the continuous casting of high carbon steels detrimentally affects the product quality. An increasing fraction of equiaxed solidification has proven most advantageous for a minimisation of these segregations. This can either be attained by decreasing the steel superheat or by the application of mould electromagnetic stirring.

In this thesis different approaches for a modelling of the equiaxed solidification are assessed. Hereby the mechanism of dendrite fragmentation is considered on the one hand, and heterogenous nucleation on the other. On the basis of these approaches, a model for a prognosis of the fraction of equiaxed solidification is implemented into an existing solidification model. With the use of parallelly conducted plant trials at a continuous casting plant, first estimates of the significance of such a model are made.

Acknowledgements

First and foremost, I would like to thank my thesis advisor DI Dr.mont. Christian Bernhard for his continuous support, the interesting discussions and the constructive comments during the completion of this work – and especially for the endurance in the phase of finishing the thesis.

Moreover, special thanks goes to all members of the *Christian Doppler Laboratory for Metallurgical Fundamentals of Continuous Casting Processes* for their widespread assistance and their helpful hints.

Lastly, I thankfully appreciate the patience and encouragement of my family during the years of my study and the time of the preparation of this thesis.

Affidavit

I hereby declare that the following diploma thesis has been written only by the undersigned and without any assistance from third parties.

Furthermore, I confirm that no sources have been used in the preparation of this thesis other than those indicated in the thesis itself.

Sebastian Ch. Michelic

Leoben, December 2006

Contents

List of Symbols

α	$[m^2\,s^{-1}]$	thermal diffusion coefficient
γ	$[rad]$	bending angle
Γ	$[m\,K]$	Gibbs-Thomson coefficient
Δl	$[m]$	longitudinal mesh spacing
Δr	$[m]$	radial mesh spacing
ΔN	$[m^{-3}]$	change in nuclei density
ΔR_e	$[m]$	growth of equiaxed nuclei in one timestep
ΔT	$[K]$	undercooling
ΔT_σ	$[K]$	standard deviation of ΔT distribution
ΔT_c	$[K]$	undercooling of columnar structure
ΔT_C	$[K]$	solutal undercooling
ΔT_N	$[K]$	mean nucleation undercooling
ΔT_R	$[K]$	curvature undercooling
ΔT_T	$[K]$	thermal undercooling
η	$[m^2\,s^{-1}]$	viscosity
κ	$[W\,m^{-1}\,K^{-1}]$	thermal conductivity
λ_1	$[m]$	primary dendrite arm spacing
λ_2	$[m]$	secondary dendrite arm spacing
ρ	$[g\,m^{-3}]$	density
ϕ	$[-]$	volume fraction (Hunt's model)
θ	$[K]$	unit undercooling

Ω	$[-]$	supersaturation
c_p	$[J\,m^{-3}\,K^{-1}]$	specific heat capacity
$C^\star$	$[wt.\text{-}\%C]$	observed (segregated) composition
$C_L^\star$	$[wt.\text{-}\%C]$	composition at dendrite tip
C_0	$[wt.\text{-}\%C]$	initial carbon composition
C_R	$[-]$	fragmentation criterion
dxt	$[m]$	length of undercooled zone
D	$[m^2\,s^{-1}]$	diffusion coefficient
D_l^γ	$[m^2\,s^{-1}]$	diffusion coefficient for austenite
f_e	$[-]$	fraction of equiaxed crystallites
f_s	$[-]$	fraction of solid
f_{sed}	$[-]$	sedimentation ratio
$F_{frag,no}$	$[-]$	fitting factor (amount of fragmented dendrites)
$F_{frag,rad}$	$[-]$	fitting factor (radius of fragmented dendrites)
$F_{trans,fs}$	$[-]$	fitting factor (transportation at fixed side)
$F_{trans,ls}$	$[-]$	fitting factor (transportation at loose side)
F_{CET}	$[-]$	fitting factor (CET transition coefficient)
g	$[m\,s^{-2}]$	gravitational constant
G	$[K\,m^{-1}]$	temperature gradient
G_C	$[K\,m^{-1}]$	concentration gradient
G_L	$[K\,m^{-1}]$	outward thermal gradient
K	$[-]$	node indication
$_k$	$[-]$	node index
k	$[-]$	equilibrium distribution coefficient
H	$[J\,m^{-3}]$	volumic enthalphy
I_{EMS}	$[A]$	stirring current
k_κ	$[-]$	multiplicative factor for the thermal conductivity
l	$[m]$	distance to meniscus
L_H	$[J\,m^{-3}]$	latent heat of solidification
m	$[K\,wt.\text{-}\%C^{-1}]$	gradient of the liquidus slope

n_f	$[m^{-3}]$	amount of possibly fragmented dendrites
n_{max}	$[m^{-3}]$	maximum nuclei density
N_0	$[m^{-3}]$	density of nuclei (Hunt's model)
N_{frag}	$[m^{-3}]$	fragmented dendrite density
N_{het}	$[m^{-3}]$	heterogenous nuclei density
N_T	$[-]$	number of nodes in the undercooled zone
p	$[-]$	complementary equilibrium distribution coefficient
P_C	$[-]$	solutal Péclet number
P_T	$[-]$	thermal Péclet number
$\dot{Q}$	$[J\,g^{-1}]$	heat flux
r	$[m]$	radial spacing, position index
R	$[m]$	dendrite tip radius
R'	$[m]$	radius
R_F	$[m]$	radius of CET position at fixed side
R_{frag}	$[m]$	radius of fragmented crystallites
R_{het}	$[m]$	radius of CET nucleated nuclei
R_L	$[m]$	radius of CET position at loose side
R_S	$[m]$	radius of caster
t	$[s]$	time
t_f	$[s]$	local solidification time
T	$[°C]$	temperature
$T^\star$	$[°C]$	temperature at dendrite tip
T_L	$[°C]$	liquidus temperature
T_S	$[°C]$	solidus temperature
$\dot{T}$	$[K\,s^{-1}]$	cooling rate
$\vec{u}$	$[m\,s^{-1}]$	velocity of melt due to stirring
u_z	$[m\,s^{-1}]$	projected velocity of the melt inside the mushy region
v_c	$[m\,s^{-1}]$	casting velocity
v_p	$[m\,s^{-1}]$	sedimentation velocity
V	$[m\,s^{-1}]$	solidification velocity

V_e	$[m\,s^{-1}]$	growth velocity of the equiaxed dendrites
V_n	$[m^3]$	volume size of element
V_T	$[m\,s^{-1}]$	speed of dendrite tip
x	$[m]$	position
x_d	$[m]$	position of dendrite tip
$\%equi_{sol}$	$[\%]$	percentage of equiaxed area

List of Figures

List of Tables

1. Introduction

In the continuous casting of high carbon steels, the formation of centre segregations is one of the most harmful defects. In the subsequent process steps centre segregations can only partially be reduced but never fully removed. Moreover additional heat treatment steps are capital intensive and increase the lead time for the product. Therefore, the minimisation or even the better control of centre segregations when casting high carbon steels is a declared aim of steel producers.

The formation of centre segregations is closely related to segregation at a microscopic scale. The solubility of most alloying elements in solid iron is comparatively lower than the solubility in liquid iron. Under nonequilibrium conditions, this leads to an enrichment of the segregating elements in the two phase region between liquidus and solidus. The segregation at the microscopic scale is termed microsegregation and related to dimensions of dendrites and grains.

Convection, caused by solutal or thermal bouyancy forces, forced convection by electromagnetic fields or a deformation of the mushy zone, results in a transport of the segregated melt at a length scale, one order of magnitude higher. The associated enrichment of the residual liquid in the centre of the strand is the reason for a steadily increasing concentration of segregating elements between the surface and the centre. In the case of a fully columnar solidification of the strand, the products' enrichment is characterised by a segregation peak in the centre – harmful for most products and difficult to remove during subsequent process steps. An early transition from columnar to equiaxed solidification proved to enhance the characteristic of the centre segregation in the continuous casting of long products (blooms or billets).

Thus, an increase of the amount of equiaxed structure is a declared objective in the further development of the continuous casting of long products. Beyond others, electromagnetic stirring in the mould and the steel superheat have been found to be the most important parameters.

Since the detailed influences of various process parameters on equiaxed solidification are hard to predict straight away, numerical simulation is a handy feature to decrease the necessary plant trials for a prognosis of the effects. Within the frame of this diploma thesis the formation of equiaxed solidification in the products of the continuous casting machine CC3 at voestalpine Stahl Donawitz GmbH & Co. KG has been studied in detail. This caster is a 5-strand round bloom caster with a diameter of 230 mm. Within the frame of a project at the *CD-Laboratory for Metallurgical Fundamentals of Continuous Casting Processes* the first step for modelling the solidification structure was carried out: the creation of thermal model for this specific bloom caster [2]. This model was thoroughly validated [3] and taken as a basis for the subsequent modelling of equiaxed solidification. Based thereupon the presented diploma thesis and a parallelly conducted Ph.D. thesis [4] have focused on examining the influences on a transition from columnar to equiaxed solidification by creating a numerical model.

In the first part of this thesis a literature review on the transition between columnar and equiaxed solidification is presented. Secondly, the theoretical basics for modelling the microstructure formation in the continuous casting process are introduced. Within the scope of the practical work of this thesis, the existing thermal model has been enhanced in order to consider the thermal effects of electromagnetic stirring – the results are displayed accordingly. Moreover, the actual implementation of the theory of microstructure formation is illustrated. Lastly, the model is used to evaluate the effect of varying casting parameters on the transition between columnar and equiaxed solidification. The results are compared to parallelly conducted plant trials in order to show the validity of the model.

All practical and numerical results have been obtained for one selected steel grade – the SB8X30N as it is called in the producer's manual. This steel grade is a high carbon prestressed concrete steel which is frequently affected by a high formation of centre segregations during production. Its composition can be found in the appendix C. Admittedly the validity of the model is therefore limited to this steel grade, however the evaluation of practical results also was only conducted for the selected grade.

2. Columnar to Equiaxed Transition in Continuous Casting

The continuous casting of special steels, especially high carbon steels, on bloom or billet casters is frequently affected by quality deteriorations owing to the formation of macro segregations in the cast strand. The formation of these defects is described by Schwerdtfeger [5] who illustrates that two different manifestations have to be considered:

Firstly, solidification structures of continuously cast products often show an anisotropy of the dendrite growth augmenting towards the centre of the strand. Often referred to as advancing solidification, nonproportionally fast growing dendrites from either side of the strand will coalesce before the solidifying fronts actually meet. Thence constricting areas which still contain liquid melt, the convection of the melt is substantially inhibited. This suppresses that melt, enriched due to the solidification segregation, can mix with less enriched melt, resulting in remarkable concentration differences. Termed mini-block formation, this phenomenon is accompanied by the formation of macro cavities since the feeding of the constricted areas is prevented. The formation of these mini-blocks is illustrated in **Fig. 2-1**, showing how local coalescence forms constricted areas which contain segregated areas.

Next to the described formation of mini-blocks and cavities, centre segregations have to be considered. Next to a segregation of carbon, the contents of phosphorus and sulphur are also observed to differ substantially from the starting composition. This is attributed to the fact that these elements have a very low distribution coefficient between liquid in melt, i. e. a high segregation coefficient. Therefore, large differences in the content of these

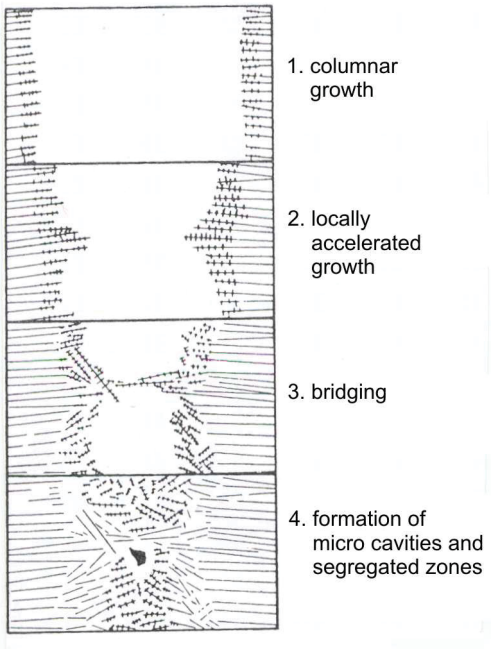

Figure 2-1.: *Sequence of mini-block formation during solidification. [5]*

elements are observed between liquid and solid. Thus segregating during solidification, the melt enriches with these elements. [1] With regard to high carbon steels, these segregations are especially harmful since they lead to the formation of cementite networks. In the further processing of the bloom these cementite networks can only partially be broken and lead to non-uniform mechanical properties.

Being extremely detrimental for the features of products on the one hand and their uniformity on the other, the reduction of centre segregations is most important.

Numerous studies [6–10] have proven that both phenomena are most effectively controlled by an equiaxed solidification of the melt, as shown in **Fig. 2-2**. In this figure the segregation index is defined as the ratio between the observed concentration of an element $C^{\star}$ and its initial content C_0: $C^{\star}/C_0$.

In contrast to the positive effects of equiaxed solidification on mini-block formation, the increased development of V-segregations with a rising fraction of equiaxed microstructure has to be mentioned. [1]

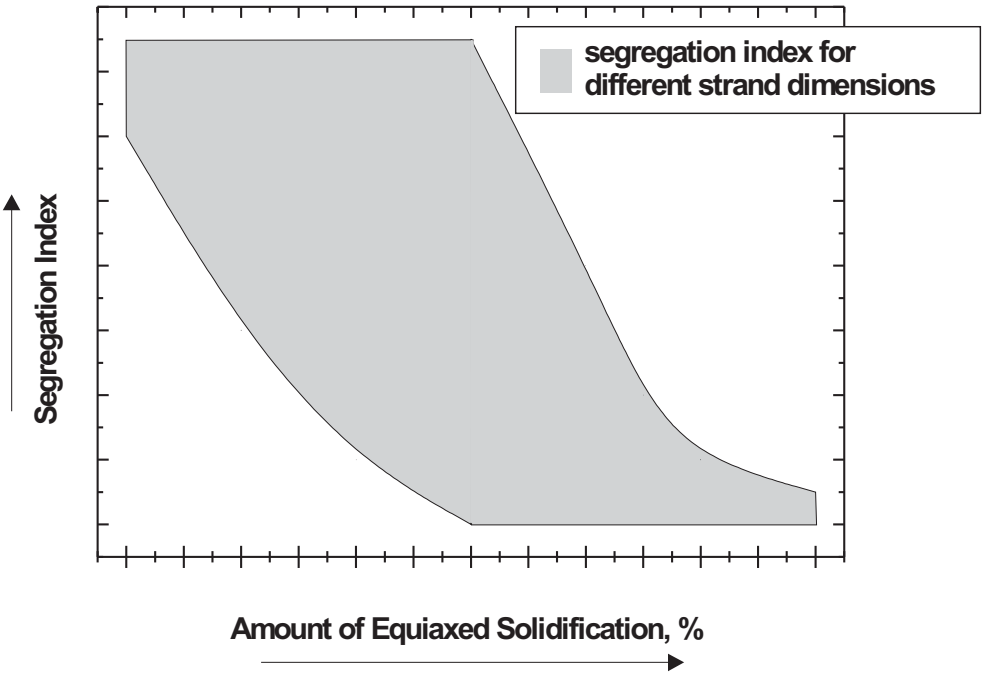

Figure 2-2.: *Influence of the amount of equiaxed solidification on the segregation index according to data from [5].*

The solidification morphology of the melt is controlled by thermodynamic and kinetic factors. The exact influential factors determining the structure of the solidification has very comprehensively been described by Kurz and Fisher [11], wherefore an exact description is neglected in this work. Shortly stated, it can be said that the solidification morphology is a function of alloy composition and its principal solidification behaviour (especially regarding eutectic solidification), the temperature gradient at the dendrite tip G and the solidification velocity of the dendrite V. Within the group of steels, the first factor is by magnitudes less influential than the latter two. Combining their influence on the morphology yields the parameter G/V. Whilst a high value of G/V results in columnar solidification, equiaxed solidification will occur if the parameter is small, as shown in **Fig. 2-3**.

Moreover, whilst a columnar solidification occurs in superheated melts with a temperature gradient ahead of the liquidus front, an equiaxed structure will only form if its surrounding is undercooled. Since continuously cast melts are on the whole superheated, the initial solidification is always columnar. Depending on the dimensions of the strand,

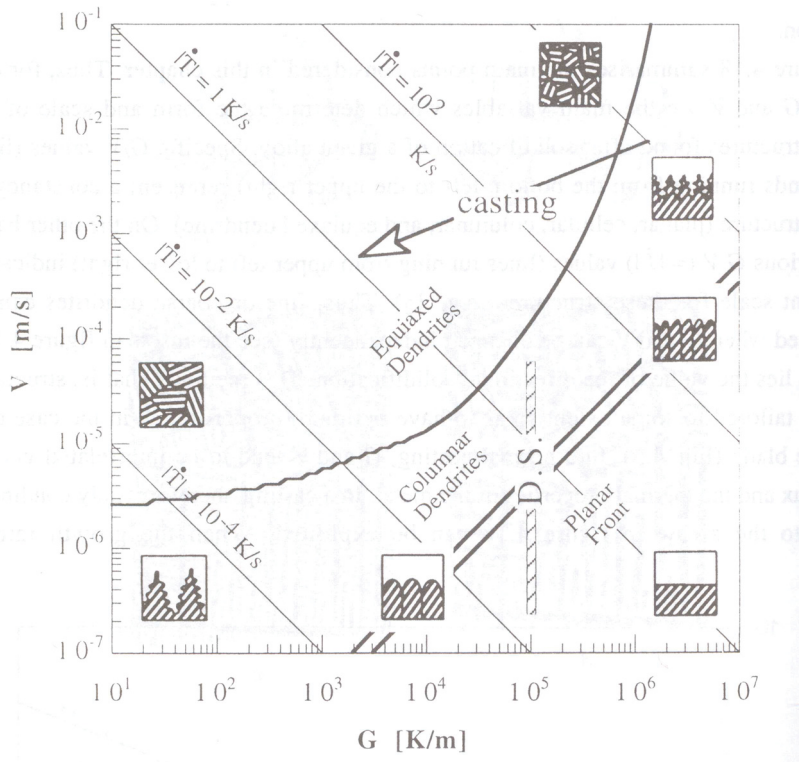

Figure 2-3.: *Solidification morphologies as functions of G and V. [11]*

a fully columnar solidification is possible. With rising strand dimensions, an equiaxed solidification in the core of the strand is more likely, owing to the low thermal conductivity of steel, resulting in a small value of G/V.

Therefore special metallurgical methods have to be applied in order to adjust conditions which promote the shifting from a columnar to an equiaxed solidification – the so-called columnar to equiaxed transition (CET). It can apparently be concluded that attaining an undercooled zone is the principle goal for reaching CET. The essential approaches are illustrated in the following section.

Lastly, it should be pointed out again that the described methods only apply to billet or bloom casting, since equiaxed solidification is not desired in slab casting.

2.1. Possibilities of Influencing CET

According to Wünnenberg [1] several possibilities of promoting an equiaxed solidification exist. In order to adjust the presence of an undercooled zone, stirring, cooling, inoculation and vibration have emerged as possibilities. Whilst the first two are regularly applied in casting practise, the last two only play a minor role, mostly for economic reasons.

2.1.1. Electromagnetic Stirring

Generally, electromagnetic stirring is a frequently applied technique in the continuous casting process. Next to the enhancement of equiaxed solidification by electromagnetic stirring in the mould, it is used in several zones of the strand for different reasons of quality improvement as illustrated in **Fig. 2-4**.

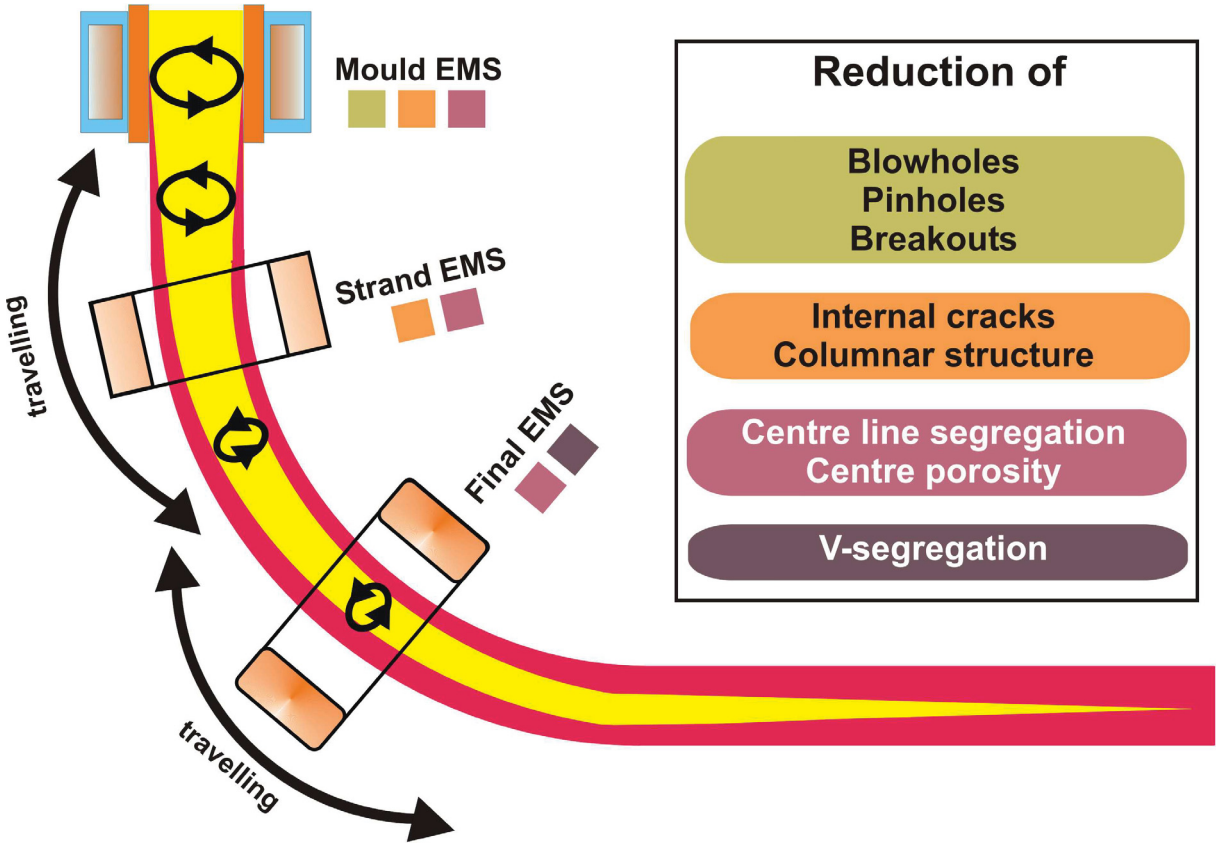

Figure 2-4.: *Possible positions of the electromagnetic stirrer and their effects on product quality.*

With regard to its influences on the CET by *mould* electromagnetic stirring, the basic idea behind this method is manifold: Through the application of a rotating magnetic field the melt inside the strand is thoroughly mixed, evening the temperature gradient resulting from the solidification. Thus the heat transfer from the liquid melt into the solid shell is increased. Even though an influence of this increased heat transfer on the overall heat flux in the mould is hardly noticeable in practise [12, 13], simulations have shown that the surface temperature of the strand in the mould increases with the application of electromagnetic stirring [14], as shown in **Fig. 2-5**.

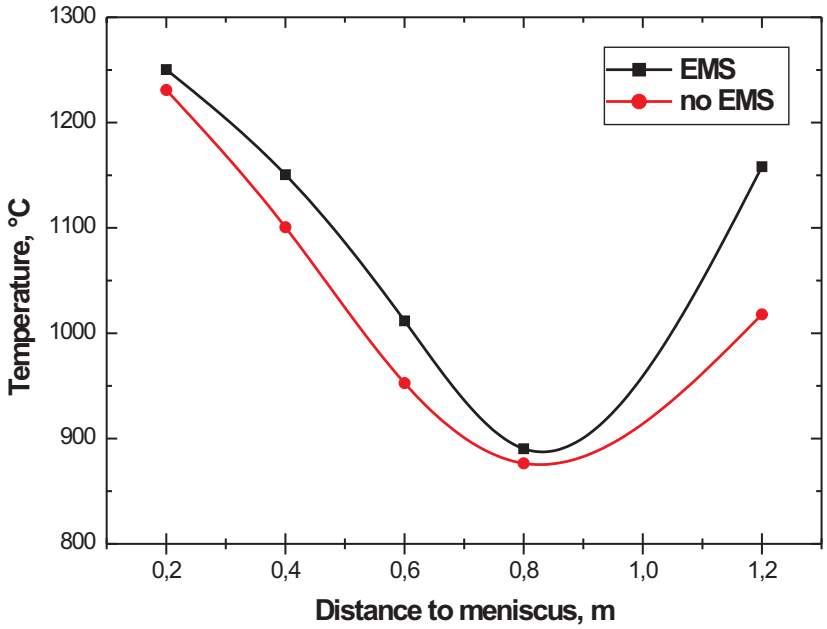

Figure 2-5.: *Influence of electromagnetic stirring on strand surface temperature [14].*

Thus increasing the heat transfer from the liquid melt into the solid shell, the process-related superheat is reduced.

Furthermore, the growing dendrites of the solid shell are exposed to the accelerated liquid melt, exerting a force on them. As an example, **Fig. 2-6** clearly shows the effects of electromagnetic stirring. Although caused by the final electromagnetic stirrer, the mechanical effects on the dendrites are similar: the primary dendrite arm is clearly bent

Figure 2-6.: *Effect of electromagnetic stirring on dendrite orientation – clearly visible the bending of the primary dendrite arms. [3]*

by app. 90 °. Since the strength of these dendrites is rather limited in the regions of mould electromagnetic stirring, several possible phenomena occur. Wünnenberg [1] has published the theory that some of the dendrite arms are torn off the dendrite stem. Although this theory is supported by different authors, recent observations have shown that the fragmentation actually occurs in a different manner.

Namely Campanella *et al.* [15] and Hellawell *et al.* [16] have – contrary to the previous perception – stated that the dendrite arms are not fragmented in the classical sense. The authors distinguish between two mechanisms whose appearance is dependent on the position in the mushy zone. Firstly, in case the hot melt is transported to positions near the primary dendrite tips where the secondary dendrite arms are not well developed, the latter are actually remelted (i. e. dissolved) by the hot melt. The second possibility occurs in deeper regions of the mushy zone where the secondary dendrites are well developed. Here the melt will locally start remelting the secondary dendrites on their linkage to the stem; effectively producing fragments. These mechanisms are schematically illustrated in **Fig. 2-7**. Furthermore, in this study [15] it was shown that the minimum distance from the dendrite tip, where the formation of clear dendrite necks can be observed, lies between 6 and $8 \cdot \lambda_2$, where λ_2 is the secondary dendrite arm spacing.

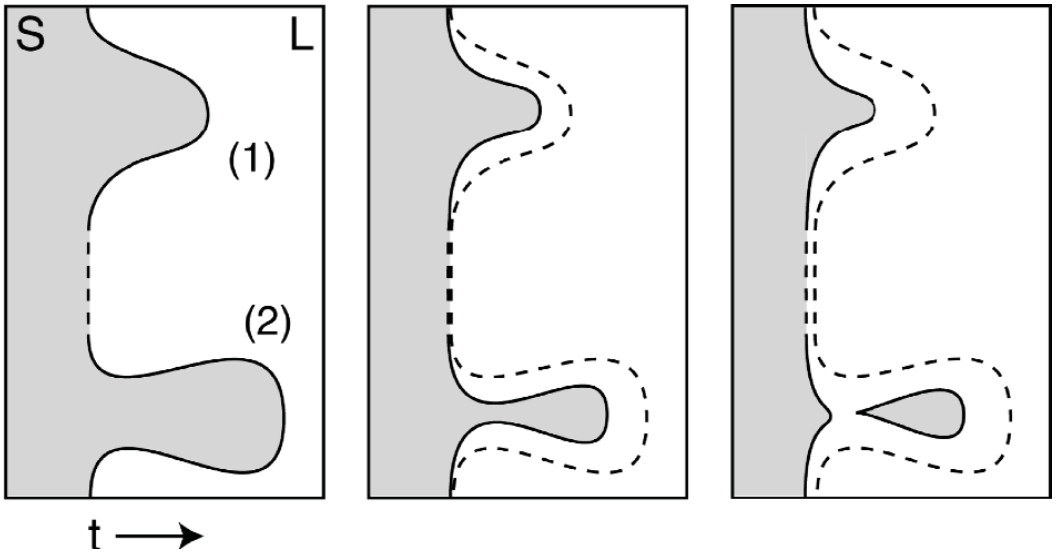

Figure 2-7.: *Influence of hot melt on the dendrite side arms – if not well developed they are remelted (1) or molten off (2). [15]*

All the same, both theories presume the existence of fragmented dendrite arm fractions before the solidification front, marked by the dendrite tip. Hence these fragmented dendrite particles will – although very small – serve as possible nucleation cites for equiaxed crystallites, clearly promoting an earlier CET. The effects of the application of electromagnetic stirring on the CET are displayed in **Fig. 2-8**.

2.1.2. Superheat

In addition to the influences of electromagnetic stirring on the CET, it is evident that a sustainable overall decrease of the melt's temperature assists the formation of equiaxed crystallites. Since the continuous casting process impossibly permits very low superheats of the melt, several experiments have been conducted in order to cool the melt either in the tundish or in the mould [1]. The tested possibilities were addition of cooling scrap in the tundish, spooling-in of steel wire or belt or the addition of special powders. However, none of these approaches have been realised on a large scale.

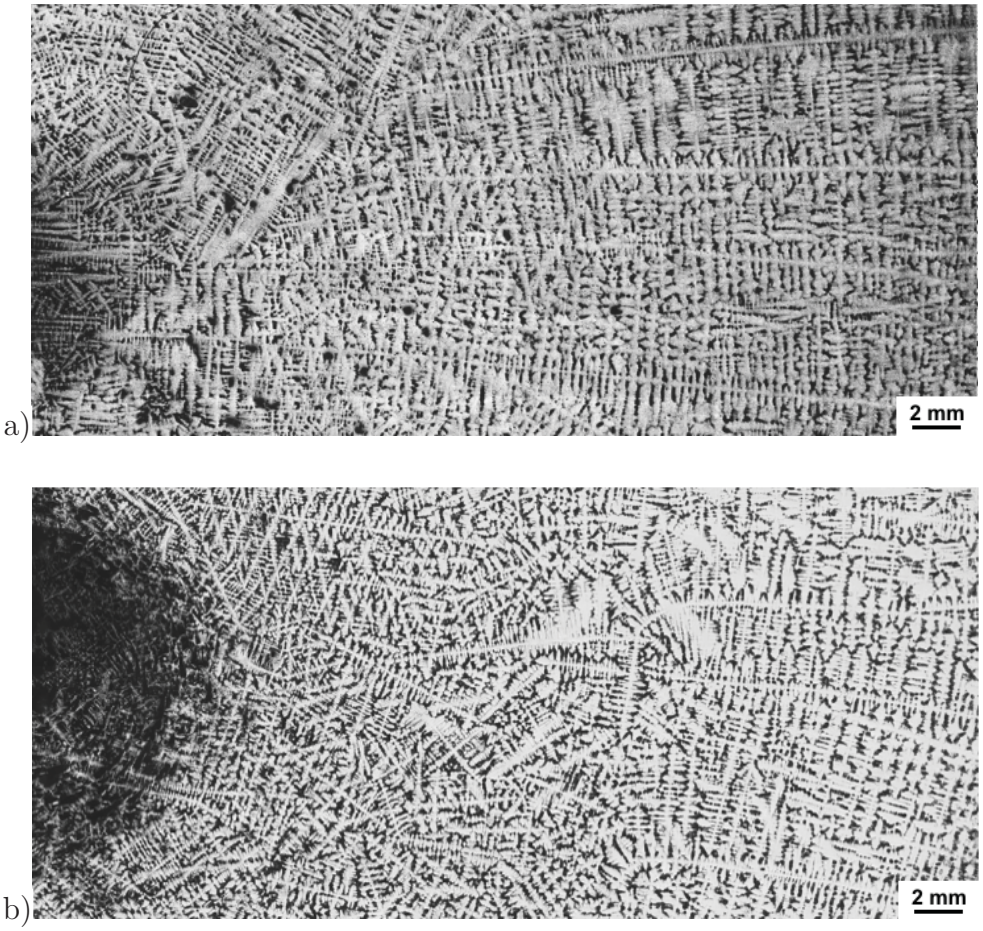

Figure 2-8.: *Solidification morphology of an unstirred bloom (a) and a stirred bloom (b) – the transition between columnar and equiaxed transition is clearly visible. Additionally the effect of the final electromagnetic stirrer on the dendrites' orientation can be seen in (b). [3]*

Since a substantial increase of the overall amount of equiaxed solidification, as illustrated in **Fig. 2-9**, is apparent, the lowest possible superheat of the melt, still allowing riskless casting, should be employed.

The influence of the superheat on the amount of equiaxed solidification has also been investigated for the continuous casting machine CC3 at voestalpine Stahl Donawitz GmbH & Co. KG [3]. The relevant results are presented in section 5.2.1 and show great consistency with the literature for low and medium superheat.

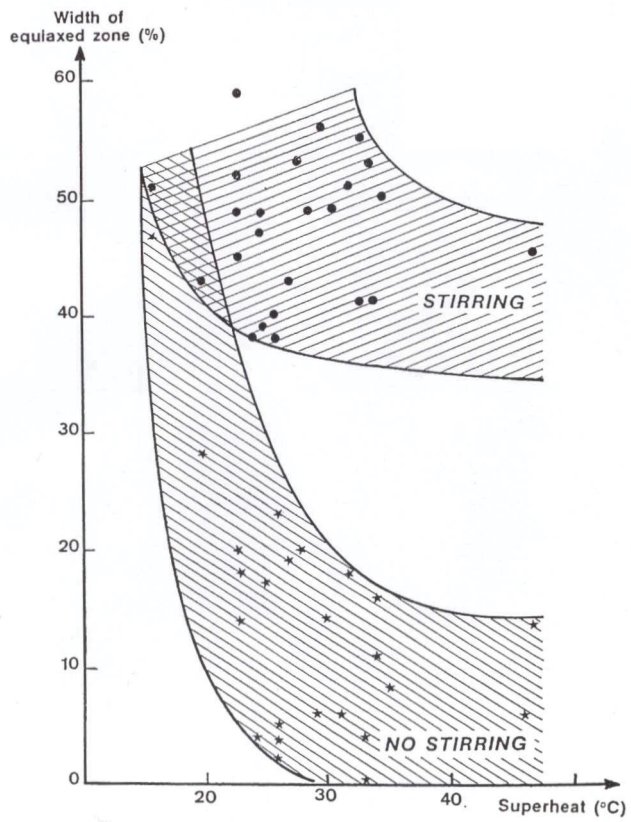

Figure 2-9.: *Influence of superheat on the amount of equiaxed solidification. [6]*

2.2. Prediction of the CET

In the past, numerous studies [6, 15, 17–20] have been carried through, bearing the modelling of equiaxed solidification as a principal aim in mind. On the other hand, only few authors [21, 22] have devoted the emphasis of their work to a clear prediction of the CET in the continuous casting process.

Nonetheless, it can be deduced from all mentioned studies that CET is not restricted to a certain point but a steady process, since columnar and equiaxed growth are concurring forms of solidification. Although clear extrema with regard to temperature gradient and solidification velocity only permit distinct solidification morphologies, a certain transition area exists, within which the columnar solidification will overweigh the equiaxed or *v. v.*. Consequently, transition conditions need to be formulated. Several authors have taken the approach of balancing reference volume elements with regard to the filling level of the

equiaxed amount. Thus detailed modelling requires the accurate description of number and size of equiaxed crystallites.

Models for a general estimation of the CET have been proposed by Frederiksson and Olsson [8], Lipton *et al.* [23] and Hunt [17], the latter of them is presented below.

2.2.1. CET Condition of Hunt

The model proposed by Hunt is valid for both, dendritic and eutectic alloys. The assumptions taken in this model are: [17, 24]

1. A stationary state is considered – this corresponds to the situations of directional solidification in a Bridgeman-type furnace.

2. Equiaxed solidification is only possible in an undercooled region, ahead of the columnar front. The nucleation rate of the crystallites is given as a function of the undercooling.

3. The criterion of CET is given by a so-called mechanical locking of the columnar grains by the equiaxed crystallites. Hunt has stated that a structure is fully columnar if the factor ϕ, the volume fraction of the equiaxed grains, is larger than 0.49. Equally, the structure is considered to solidify columnarly when ϕ is equal to 1 % of the above value, indicating the equiaxed crystallites are entrapped by the columnar grains.

Based on these assumptions, the following estimation of equiaxed growth can be made: Considering equiaxed grains to have nucleated at time $t = 0$ at a given undercooling ΔT_N, together with ΔT_c as the undercooling of the columnar structure, yields the subsequent condition for equiaxed solidification,

$$G < 0.617 \cdot N_0^{1/3} \cdot \left(1 - \frac{\Delta T_N^3}{\Delta T_c^3}\right) \Delta T_c \tag{2-1}$$

where N_0 is the density of equiaxed nuclei. The above expression has been derived by the stated assumptions together with several conversions [17] which are omitted for reasons

of clarity. The basic message which should be derived from **equation (2-1)**, is that with Hunt's model the CET is mainly a function of the temperature gradient. Obviously the afore mentioned mechanisms like dendrite fragmentation are not considered in this model, wherefore Hunt's model is only conditionally apt for estimating the CET in the continuous casting process.

In the subsequent chapter a possible approach to modelling the CET in the continuous casting process will be presented. Although necessitated before, the presented model will not include the overall description of the mentioned thermal model, since this has been subject of previous projects and has adequately been explained there [2, 25–27]. However, since solidification is always linked to changes in temperature and enthalpy, the concepts as far as deemed necessary, will be illustrated.

3. Modelling the Columnar to Equiaxed Transition

In the following, the necessary concepts for modelling the CET with relevance to the continuous casting process will be presented. Firstly however, it has to be stated that the presented model only applies for the 1-domain method. Therefore solid and liquid media are considered as one medium, their distinction achieved by temperature and enthalpy fields. The idea behind these methods is that a simple relationship between temperature and enthalpy or fraction of solid exists, in order to solve the heat flow equations with latent heat release owing to solidification.

With regard to a macroscopic perception of the whole system these assumptions suffice, however with regard to microstructure formation (i. e. microscopic view), basic mechanisms of nucleation and growth of crystallites need further attention. For this reason the required concepts for a macroscopic modelling of the solidification phenomena is shortly discussed, whilst the different theories for the microscopic events are illustrated fully.

3.1. Solidification and Enthalpy Changes

At the scale of the entire continuous casting process, solidification is primarily controlled by heat diffusion. Moreover a clear influence of convection in the liquid is observed – its description can be obtained elsewhere [20]. With regard to heat diffusion, the following dependency for both liquid and solid can be stated:

$$\operatorname{div}\left[\kappa(T)\cdot\operatorname{grad}T(r,t)\right]+\dot{Q}=c_p(T)\cdot\frac{\partial T(r,t)}{\partial t} \tag{3-1}$$

It becomes clear from this equation that the essential material parameters κ and c_p are temperature dependent. $\dot{Q}$ represents the change in heat of the system resulting from latent heat release due to phase transformation,

$$\dot{Q}=L_H\cdot\dot{f}_s(r,t) \tag{3-2}$$

where $\dot{f}_s$ is the change in fraction of fraction of solid f_s in a given time interval. Based on these two equations, two different continuations can be found in the literature: the equivalent specific heat method and the enthalpy method [28]. The application of the latter is more suitable when dealing with solidification calculations for a number of reasons. Firstly, energy conservation is ensured, and secondly any solidification path is characterised by strictly decreasing enthalpy (even during recalescence), which is important when dealing with equiaxed solidification. [20] With the application of this method the volumic enthalpy H is introduced:

$$H(T)=\int_0^T c_p(T')\mathrm{d}T'+L_H\cdot\big(1-f_s(T)\big) \tag{3-3}$$

Combining equations **(3-1)-(3-3)** hence yields:

$$\operatorname{div}\left[\kappa(T)\cdot\operatorname{grad}T(r,t)\right]=\dot{H}\left[T(r,t)\right] \tag{3-4}$$

The necessary relationships for $H(T)$, $c_p(T)$ and $f_s(T)$ can be deduced from the adequate databases, or – and more reasonably – by implementing a model for coupled calculation of micro segregation and/or thermodynamics. The use of such a model allows the consideration of segregation effects due to concentration difference and diffusion-processes in the liquid and/or solid resulting from solidification. However, such models are very complex (especially the thermodynamic calculations) wherefore the firstly stated approach is frequently chosen. It should however be noted that a complete negligence of segregation

effects owing to solidification, would make the subsequent modelling of equiaxed solidification superfluous. Therefore some form of segregation model has to be considered, since it strongly influences the liquidus temperature of the steel.

With regard to outer effects on the system, equation **(3-4)** needs to be altered by appropriate approaches for Dirichlet, Neumann or Cauchy conditions. However, their consideration is not causal with the subsequently microscopic modelling, wherefore only reference to suitable publications is given [20, 29].

3.2. Microstructural Modelling

In the presented model is it assumed that a thermodynamic database is used for computing the above stated necessary parameters. The goal of the model is therefore to predict the microstructural parameters and grain structures arising during solidification, requiring the knowledge of the thermal history of the strand. With the thermal history being known, it is possible to calculate the cooling rate, thermal gradient, solidification rate and local solidification times at all locations in a given mesh. The microstructural parameters can hence be deduced in an *a-posteriori*-method of the thermal results.

The necessary parameters from the thermal results are presented in the following. Firstly, the temperature gradient at the dendrite tip G for each timestep must be calculated:

$$G = \operatorname{grad} T(x,t)_{T=T_L} \tag{3-5}$$

The second necessary parameter is the solidification velocity V, estimated by the following quotient:

$$V = \left(\frac{\frac{\partial T(x,t)}{\partial t}}{\operatorname{grad} T(x,t)} \right)_{T=T_L} \tag{3-6}$$

The cooling rate $\dot{T}$ is the product of the last two parameters:

$$\dot{T} = G \cdot V \tag{3-7}$$

Lastly the local solidification time t_f is essential for any microstructural calculations:

$$t_f = \frac{T_L - T_S}{\dot{T}} \tag{3-8}$$

3.2.1. Columnar Growth

Since thermodynamic databases for steel always assume columnar dendritic solidification, their application brings along that in a given thermal history the exact position of the liquidus and solidus isotherms is known. However, during the advance of the columnar dendritic front, solute is rejected ahead of the solidification interface. The change of concentration ahead of the interface will affect the local equilibrium solidification temperatures. Therefore the position of the liquidus isotherm is not consistent with the exact position of the tip. The advancement of the isotherms constrains the dendrite growth velocity which in turn determines the tip undercooling. Since it is assumed that the formation and growth of equiaxed crystallites takes place in this zone of undercooled melt (i. e. the distance between T_L and the actual position of the dendrite tip), special attention is devoted to calculating the tip undercooling.

Hunt *et al.* [30] have shown that the tip undercooling for low solidification velocities can be approximated by:

$$\Delta T = \frac{G \cdot D}{V} \tag{3-9}$$

This model assumes that the tips are growing at the limit of stability and no constitutional undercooling occurs ahead of the dendrite front. Since a constitutionally undercooled zone always exists at the dendrite tips, this approach is not applicable. [31]

Various other models have been proposed in the literature for the description of the dendrite tip undercooling. These models mainly differ in two aspects: the dendrite growth criterion (maximum velocity vs. stability limit) and the shape of the tip (half-sphere vs. paraboloid of revolution). According to Etienne [21], the model proposed by Kurz and Fisher [11] seems most applicable for continuous casting steel.

The authors describe several models for the dendrite tip undercooling ΔT, wherefrom the model for constrained alloy dendrite growth is illustrated since it represents the case of continuous casting. Owing to the constrained growth, the latent heat generated during solidification flows into the solid and not the liquid. Therefore the thermal contribution to the tip diffusion fields can be neglected. The total tip undercooling is hence described by:

$$\Delta T = \Delta T_C + \Delta T_R \tag{3-10}$$

The first contribution to this equation, the solutal undercooling ΔT_C, results from the concentration changes ahead of the dendrite tip. Assuming a tip concentration of $C_L^\star$ and a constant gradient of the liquidus isotherm m, the solutal undercooling results as:

$$\Delta T_C = m \cdot (C_0 - C_L^\star) \tag{3-11}$$

The definition of the solutal supersaturation,

$$\Omega = \frac{C_L^\star - C_0}{C_L^\star \cdot p} \tag{3-12}$$

where p is the complementary equilibrium distribution coefficient $p = 1 - k$, yields the following expression for ΔT_C:

$$\Delta T_C = m \cdot C_0 \cdot \left(1 - \frac{1}{1 - \Omega \cdot p}\right) \tag{3-13}$$

According to Kurz and Fisher, the supersaturation Ω was found to be

$$\Omega = I(P_C) \tag{3-14}$$

where $I(P_C)$ is the Ivantsov function as a mathematical solution of the diffusion problem for a paraboloid and P_C is the Péclet number for solute diffusion:

$$P_C = \frac{V \cdot R}{2D} \tag{3-15}$$

The calculation of the Ivantsov function is illustrated in appendix B. The second contribution to the total undercooling, the curvature undercooling, is determined by the following relationship,

$$\Delta T_R = \frac{2\Gamma}{R} \tag{3-16}$$

where Γ is the Gibbs-Thomson parameter, defined as the ratio of the specific liquid-solid interface energy to the melting entropy. From equations **(3-15)** and **(3-16)** it is obvious that for calculating the total undercooling the dendrite tip radius R is required. A criterion by Langer *et al.* [32] is based on the condition of marginally stable tip growth. The criterion postulates that the dendrite tip will grow at the margin of stability where the radius of the tip is equal the wavelength of the fastest growing instability λ_C:

$$R = \lambda_C = 2 \cdot \pi \sqrt{\frac{\Gamma}{m \cdot G_C - G_L}} \tag{3-17}$$

where G_L is the outward thermal gradient at the tip in the liquid with

$$G_L = \frac{\theta \cdot P_t}{R} \tag{3-18}$$

$$\theta = \frac{L_H}{c_p} \tag{3-19}$$

$$P_t = P_C \cdot \frac{D}{\alpha} \tag{3-20}$$

$$\alpha = \frac{\kappa}{c_p} \tag{3-21}$$

and G_C is the concentration gradient ahead of the advancing dendrite:

$$G_C = -\frac{2P_C \cdot p \cdot C_0 \cdot A(P_C)}{R} \tag{3-22}$$

In equation **(3-17)** the factor of $2 \cdot \pi$ results from a stability constant which has been introduced by Mullins and Sekerka [33].

The necessary constant factors for solving equations **(3-10)**–**(3-22)** are shown in **Tab. 3.I.**. From the illustrated model it can be deduced that for the given constants the undercooling

is ultimately only a function of the growth velocity V and the carbon content C_0 (when modelling the columnar solidification of austenite).

Table 3.I.: *Constant factors for modelling columnar solidification of austenite [11].*

Quantity	Value	Unit
Γ	19×10^{-6}	$m\,K$
D_l^γ	2×10^{-8}	$m^2\,s^{-2}$
k	0.35	
m	-62.3	$K\,wt.\text{-}\%C^{-1}$

3.2.2. Equiaxed Crystallite Formation

Depending on the thermal field, equiaxed crystallites tend to form in the undercooled zone ahead of the columnar front. These grains can originate either heterogenous nucleation (external source) or fragmented dendrites (intrinsic source). Even though Hellawell *et al.* [16] state that heterogenous nucleation can only occur once effective nucleation substances are added to the melt, this perception is in great contrast to other studies [15, 21], clearly stating that both external and intrinsic sources are responsible for equiaxed solidification in continuous casting.

3.2.2.1. Fragmentation

Hellawell *et al.* [16] have defined several steps for a cycle of equiaxed grain formation induced by convection. This perception has been adopted by Campanella *et al.* [15]. The relevant steps for dendrite arm fragmentation are:

Step I – fragmentation of dendrite necks by local remelting: As it has been explained in section 2.1.1, the opinion that the dendrites break mechanically is not supported by Hellawell *et al.*. In a preceding study [34] Hellawell and co-workers have estimated that the dendrites may be bent plastically, however actual break-off due to the bending moments are rarely observed. In order to promote local remelting of

the secondary dendrite arms, transient solidification conditions are necessary. Most important in this case is firstly a falling temperature gradient, and secondly a decrease in solidification velocity – both conditions prevailing in continuous casting. A change in these conditions causes an increase in the primary dendrite arm spacing, facilitating the sweeping effect of the stirred melt.

Step II – transportation of fragments through the mushy zone: In order to promote the transport of the fragments into the open liquid region, fluid flow by natural convection and/or induced stirring is essential. Natural convection can occur due to the density variations caused by temperature and composition changes. However, assuming the presence of a certain degree of turbulence originating electromagnetic stirring, a certain fraction of the fragmented dendrites will definitely be transported to the undercooled zone and/or the liquid melt.

Step III – survival of fragments in the liquid: The survival of the fragments ahead of the columnar front eventually depends on their actual position. While fragments within the undercooled zone will not only survive but even grow, those that are swept in the hotter liquid will start dissolving. However, since the size of these fragments is reported to range between 5 and 20 μm, their lifetime in the melt which is superheated by several degrees is comparatively short. Hellawell *et al.* [16] have reported lifetimes of less than 10 s, wherefore such particles are unlikely to become sources of equiaxed solidification.

In order to define a limit at which fragmentation of the dendrite arms will occur, an approach by Campanella *et al.* [15] is employed. The authors define that local remelting of the dendrites can only take place once the projected velocity of the stirred liquid $\vec{u}_z$ is larger than the speed of the liquidus isotherm V (respectively the isotherm of the undercooled melt, i. e. the dendrite tip, termed V_T). Hence a fragmentation criterion C_R can be defined:

$$C_R = \frac{|\vec{u}_z|}{V_T} > 1 \tag{3-23}$$

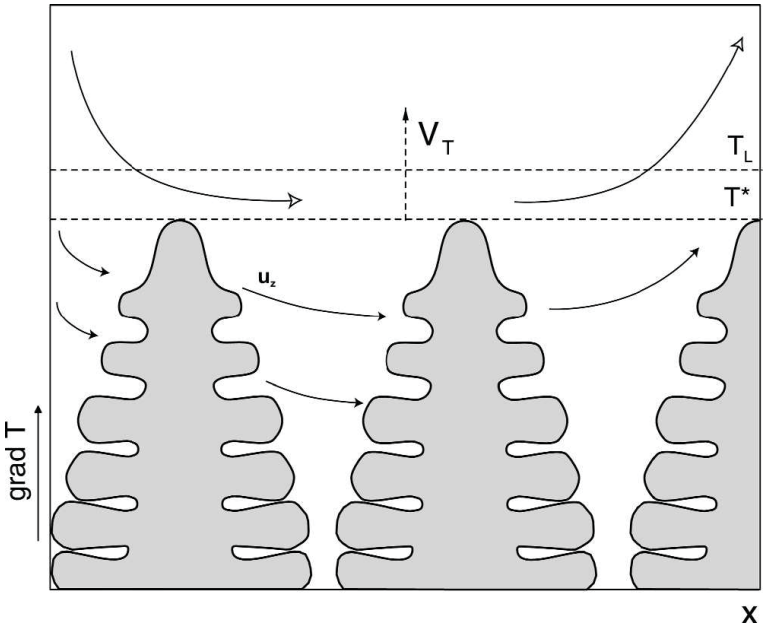

Figure 3-1.: *Schematic illustration of the interaction between fluid flow u_z and growth velocity V_T. [15]*

Given that the speed of the stirred melt at the dendrite tip is called $\vec{u}$, the share of the vector which is parallel to the temperature gradient $\vec{u}_z$ is defined by,

$$\vec{u}_z = \vec{u} \cdot \tan\beta \quad \text{with} \quad \cos\beta = \frac{\lambda_1}{r(x_d)} \tag{3-24}$$

where $r(x_d)$ is the position of the dendrite tip. The conditions for this criterion are illustrated in **Fig. 3-1**.

Given that fragmentation is possible, i. e. $C_R > 1$ the amount of possibly fragmented secondary dendrite arms is given by,

$$n_f = \frac{4}{\lambda_1^2 \cdot \lambda_2} \tag{3-25}$$

under the assumption that each primary dendrite arm forms exactly 4 secondary arms [7]. With regard to the actual number of fragmented arms, results in the literature differ widely. Harada *et al.* [35] report a quantity of 14 % of the overall amount, while Etienne [21] observes 8 crystallites $cm^{-2}s^{-1}$ with a defined radius. Lesoult *et al.* [6] have proposed the same value for the stirred regions and 4 crystallites $cm^{-2}s^{-1}$ in unstirred

regions. With regard to numerous unknown quantities, this problem cannot be solved analytically. Therefore the implementation of a fitting factor $F_{frag,no}$ is adopted in the course of this model, eventually yielding a dendrite density $N_{frag}(t) = n_f \cdot F_{frag,no}$ as a function of time.

Lastly, it should be mentioned that for an even more precise description of the fragmentation phenomena the amount of solid which is remelted due to the contact with the hot melt requires careful treatment. Employing equation **(3-4)** the change in enthalpy due to these procedures needs to be considered on a macroscopic scale.

3.2.2.2. Heterogenous Nucleation

Next to the formation of equiaxed crystallites due to fragmentation, heterogenous nucleation in the undercooled zone needs to be treated more precisely. Numerous studies have treated heterogenous crystallite formation in great detail, a suitable description can be found in [18]. Previous studies conducted by Hunt [17], Dustin and Kurz [36] and Hellawell [37] use a heterogenous nucleation law with an extinction factor to limit nucleation. However, Thévoz *et al.* [18] report that this criterion fails to replicate experimental observations, which show that the range of undercooling, within which the density of grains increases substantially, is very narrow. Therefore, Thévoz [38] has developed a nucleation model which is basically summarized in **Fig. 3-2**.

In this model the grain density is given by the integral of the nucleation site distribution from zero to the undercooling ΔT_1 (**Fig. 3-2b**). In **Fig. 3-2a** the respective integrals are depicted for a given undercooling ΔT.

The distribution of nuclei can be approximated by a GAUSSian distribution using a mean nucleation undercooling ΔT_N, the standard deviation of the distribution ΔT_σ and the maximum density n_{max}, given by an integral from zero to infinite undercooling. Hence

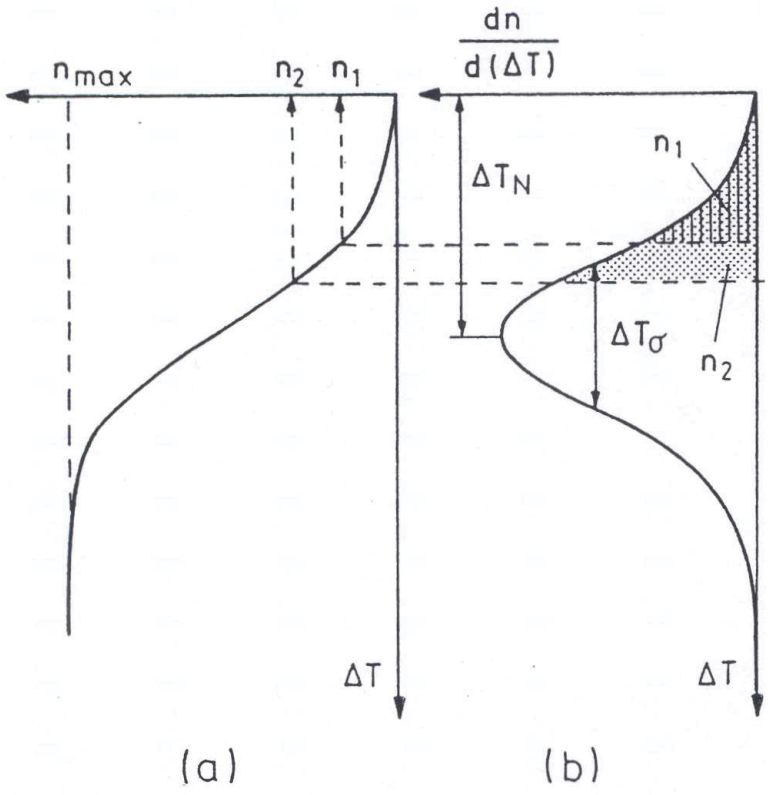

Figure 3-2.: *Nucleation model for equiaxed solidification – the density of nuclei n_1 (a) is given by the integral of the distribution (b). [38]*

$$N_{het} = \frac{\mathrm{d}n_{het}}{\mathrm{d}t} = \frac{\mathrm{d}n_{het}}{\mathrm{d}\Delta T(x,t)} \cdot \frac{\mathrm{d}\Delta T}{\mathrm{d}t} = \frac{\mathrm{d}\Delta T}{\mathrm{d}t} \cdot \left[\frac{1}{\Delta T_\sigma \cdot \sqrt{2 \cdot \pi}} \cdot \mathrm{e}^{\frac{-(\Delta T(x,t) - \Delta T_N)^2}{2 \cdot \Delta T_\sigma^2}} \right] \cdot n_{max} \qquad (3\text{-}26)$$

yields the grain density for a given undercooling $\Delta T(x,t)$. Since values for ΔT_N, ΔT_σ and n_{max} are hardly published in the literature, they can only be determined experimentally for each composition. However, without nearer specification of their source of origin, Etienne [21] has given the following parameters for a 0.75 $\%C$-steel: $\Delta T_N = 6.5\ K$, $\Delta T_\sigma = 0.8\ K$ and $n_{max} = 1.5 \times 10^{16}\ m^{-3}$.

In the same manner as done in the previous section, the nucleated equiaxed crystallites should again be considered in the enthalpy balance of equation **(3-4)**.

3.2.3. Growth of Equiaxed Crystallites

All equiaxed crystallites that have either been fragmented and transported, or heterogeneously nucleated in the undercooled zone, will start growing, due to the undercooling as a driving force. From a morphological point of view, these crystallites will again develop dendrite arms when growing. A very useful model for describing the growth of equiaxed crystallites has been proposed by Lipton, Glicksman and Kurz (LGK) [39], which is generally based on the following assumptions:

1. The dendrites grow steadily into an undercooled melt of constant undercooling.
2. The shape of the dendrite tips is described by a paraboloid of revolution (i. e. isothermal and isoconcentrate tip) – cf. section 3.2.1.
3. Convection within the liquid is neglected – heat and mass transport are only controlled by diffusion.

With regard to the undercooling as the driving force, ΔT is approximately equal to the thermal undercooling in pure substances. When considering alloys, the situation is more complex, as can be seen in **Fig. 3-3**. Bearing section 3.2.1 in mind, the total undercooling is not only composed of the curvature undercooling $\Delta T_R = [T_L(C_0) - T_L(R)]$ and the chemical undercooling $\Delta T_C = [T_t(R) - T^\star]$ but also the thermal undercooling $\Delta T_T = [T^\star - T_\infty]$. Hence

$$\Delta T = \Delta T_T + \Delta T_C + \Delta T_R \tag{3-27}$$

is valid, where the thermal undercooling can – similar to the chemical undercooling – again be expressed through the Ivantsov solution by:

$$\Delta T_T = \theta \cdot I(P_T) \tag{3-28}$$

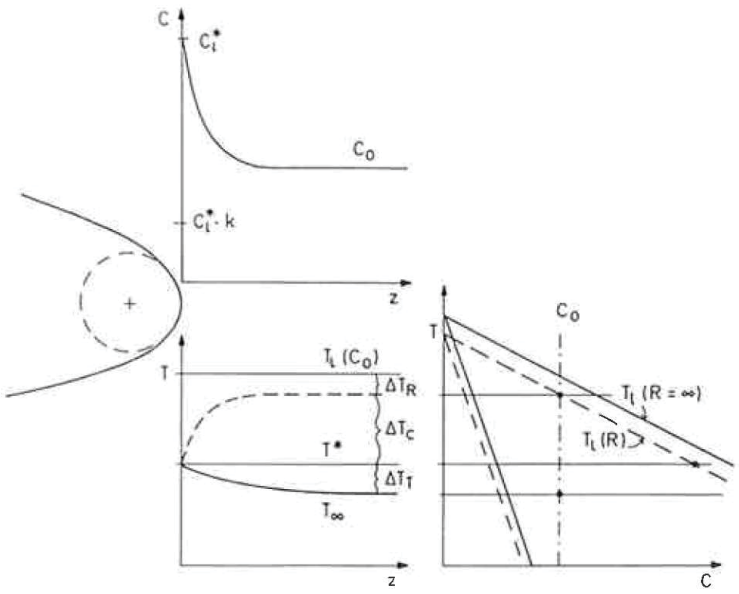

Figure 3-3.: *Diffusion fields and undercoolings at an equiaxed dendrite tip growing into an undercooled melt. [39]*

For the chemical and the curvature undercooling equations **(3-13)** and **(3-16)** are again valid. Summarizing equations **(3-17)-(3-22)** yields the following expression for the necessary dendrite tip radius R:

$$R = 2 \cdot \pi \cdot \Gamma \cdot \left[\theta \cdot P_T - \frac{2 \cdot P_C \cdot m \cdot C_0 \cdot (1-k)}{1-(1-k) \cdot I(P_C)} \right]^{-1} \tag{3-29}$$

Ultimately the growth velocity V_e can be deduced from the definition of the thermal Péclet number:

$$V_e = \frac{2 \cdot \alpha \cdot P_T}{R} \tag{3-30}$$

It has to be stated that this proposed model is only valid for small Péclet numbers (< 1), meaning that for a given composition C_O and undercooling ΔT the radius R and finally the growth rate V_e can be deduced. High Péclet numbers are not treated here since they are not relevant for the continuous casting process.

Nonetheless, it should be pointed out that the model leads to implausibly high growth rates in absence of a micro segregation model (i. e. the composition of the undercooled

zone is considered constant). With regard to the growth rate of the equiaxed crystallites it is therefore inevitable to consider the changes in liquidus temperature in the segregated melt.

Moreover, the change in the overall amount of fraction of solid needs consideration in equation **(3-4)**.

3.2.4. Transportation of the Formed Nuclei

From basic physical reflections it can be seen that the formed nuclei will not remain static within the melt. Very much in turn, observations made at the CC3 indicate a clear difference in CET for the fixed and loose side of the strand. Since these differences cannot be generated differences other than transportation phenomena, a clear indication therefor is given.

3.2.4.1. Natural Transportation

The formed crystallites will not only be moved inside the liquid because of the previously mentioned thermal and chemical gradients but also because of natural transportation owing to their size. Since the nuclei eventually reach considerable sizes they will start to be accelerated downwards by gravitation. According to the law of STOKES the fluid within which the particles are moved downwards counteracts the gravitational force by friction.

Since STOKES' law only considers spherical bodies, the behaviour of the equiaxed crystallites is approximated by a spherical contour. Hence the sedimentation velocity v_p can be expressed by

$$v_p = \frac{2 \cdot R'^2 \cdot \mathrm{g} \cdot (\rho_p - \rho_L)}{9 \cdot \eta} \tag{3-31}$$

where g is the gravitational constant, ρ are the respective densities and η is the viscosity of the fluid. Thus the nuclei are moved downward not only by the speed of the strand but

additionally according to STOKES' law. However, since the strand is bent, the angle γ at which the gravitational force acts upon the nuclei also needs to be considered. Therefore the particles will not only be transported strictly downwards but will also experience a radial translation. The sedimentation velocity is hence split into a radial and a transversal part:

$$v_{p,r} = \frac{2 \cdot R'^2 \cdot \mathrm{g} \cdot (\rho_p - \rho_L)}{9 \cdot \eta} \cdot \sin(\gamma) \tag{3-32}$$

$$v_{p,t} = \frac{2 \cdot R'^2 \cdot \mathrm{g} \cdot (\rho_p - \rho_L)}{9 \cdot \eta} \cdot \cos(\gamma) \tag{3-33}$$

3.2.4.2. Sedimentation Effects

Owing to the bending of the strand, nuclei which move downwards faster than the strand does, will start sedimenting in the fixed side of the strand, as it can be seen in **Fig. 3-4**. On the other hand, nuclei coming from the loose side will move into hotter regions of the strand and will most likely be remelted. Consequently, it is expected that the nuclei density decreases on the loose side and increases on the fixed side.

Evidently the amount of in- or decrease is given by the ratio of the sedimentation velocity to the strand velocity f_{sed},

$$f_{sed} = \frac{v_{p,t}}{v_c} \tag{3-34}$$

where v_c is the casting velocity.

3.2.5. The Actual Transition

With regard to the actual CET, several authors [21, 22] propose to determine the volume fraction of the equiaxed crystallites again by approximating the nuclei to be spherical. Evidently for this balance, both fragmented and heterogeneously formed nuclei and their respective radius have to be considered. Thus

$$f_e = \frac{4}{3} \cdot \pi \cdot \left(N_{het} \cdot R_{het}^3 + N_{frag} \cdot R_{frag}^3 \right) \tag{3-35}$$

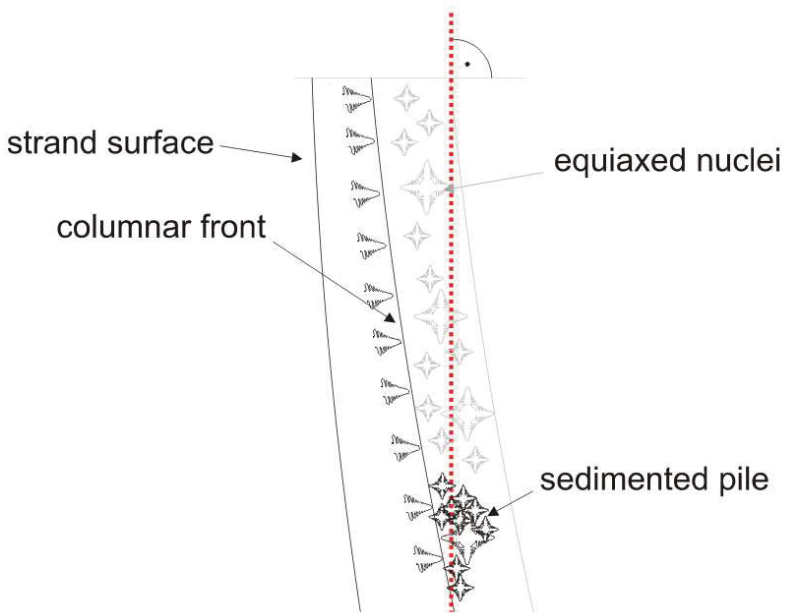

Figure 3-4.: *Sedimentation effects during continuous casting owing to the bending of the strand.*

is valid where f_e is the fraction of equiaxed crystallites, and the indices $_{frag}$ and $_{het}$ term the fragmented and heterogenous nuclei respectively. Once f_e has reached a critical level, the equiaxed crystallites will outweigh the columnar solidification and the transition has taken place. Whilst Etienne [21] proposes a critical value of 0.74 (resulting from the closest possible arrangement of spheres), Gnauck [22] proposed a CET at $f_e = 0.5$.

Given that there is no physical basis for calculating f_e, this value can only be determined by comparing calculated results with experiments.

4. Implementation of the Model

4.1. Thermal Consideration of Electromagnetic Stirring

In a first step, the existing thermal model of the CC3 was adopted in order to take the effects of electromagnetic stirring into account. Since all further calculations are limited to the initially mentioned steel grade, all shown results refer to the same. It has been explained that from a thermal viewpoint, stirring the melt decreases the differences in temperature by increasing the heat transfer between hotter and colder melt. Considering only the temperature distribution within the strand, a similar behaviour can be mirrored by increasing the thermal conductivity of the liquid by a given factor. According to numerous studies [40, 41], this idea is frequently applied if the focus of simulations lies only on the temperature distribution and not fluid dynamics. Typical amounts of this coefficient range at a value of 3 [41].

However, the published magnitudes of increase of the thermal conductivity seem rather arbitrarily chosen. Moreover, constant factors are employed, hardly reflecting the different stirring intensities over the length of the stirred region. Obviously the degree of mixing – *ergo* the strength of temperature levelling – is directly related to the velocity of the melt. Therefore it seems obvious to take the speed of the melt as a basis for a function of the conductivity increase. The velocity itself is rather hard to measure, however it is proportional to the magnetic force induced by the stirrer. This relation has been closely examined by Spitzer [42] and is the basis for a correlation of the two quantities.

In order to quantify the magnetic force, extensive measurements with a HALL-probe for different stirring currents were performed at the caster. During electromagnetic stirring,

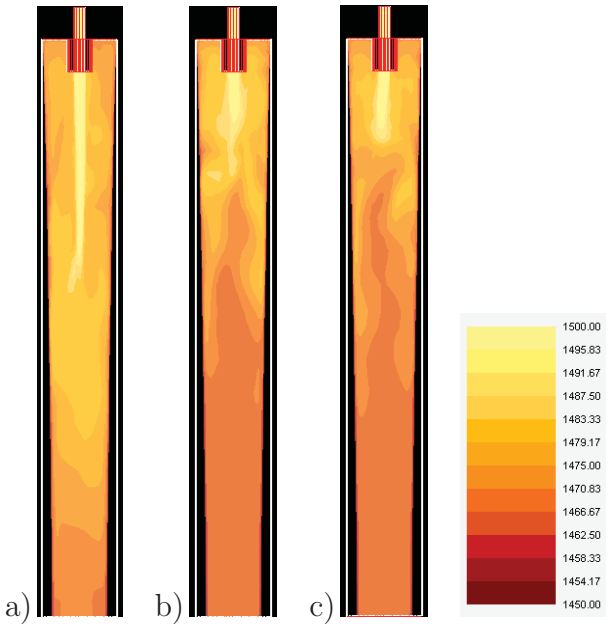

Figure 4-1.: *Cross sections of the simulated strand – temperature profile for a stirring current of (a)* 0 *A, (b)* 150 *A and (c)* 250 *A.*

the stirring current is the only variable which influences the effeciency of the stirrer. Based on Spitzer's model it was possible to implement a coupled thermofluid simulation in the commercial software CALCOSOFT-3D [4]. The clear differences of the temperature and fluid distribution of a stirred and an unstirred strand are visible in **Fig. 4-1** and **4-2**. As it has been mentioned in section 2.1.1, it is interesting to note that electromagnetic stirring leads to a considerable increase of the strand surface temperature, as displayed in **Fig. 2-5**. Moreover noticeable differences of the temperature over the cross section of the liquid can be observed, as shown in **Fig. 4-3**. It becomes clear from **Fig. 4-3** (a) and (b) that electromagnetic stirring cushions the steep temperature gradient in the centre of the strand resulting from the instreaming melt coming from the submerged entry nozzle especially in the top part of the mould. The temperature decrease in the lower part of the mould results from an upward drag of colder melt from lower parts in the strand – a phenomenon which can also be observed in **Fig. 4-1**. As a result of these simulations, it was possible to determine the velocity of the melt at the phase boundary solid/liquid – the basis for adjusting the thermal conductivity.

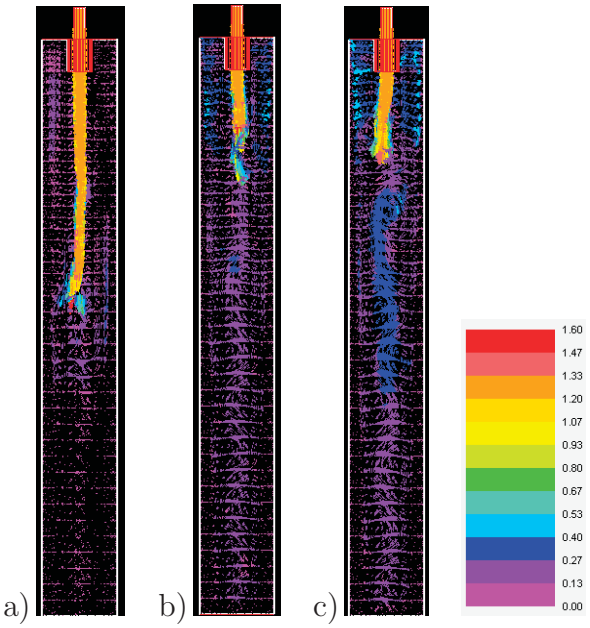

Figure 4-2.: *Cross sections of the simulated strand – velocity profile for a stirring current of (a)* 0 *A, (b)* 150 *A and (c)* 250 *A.*

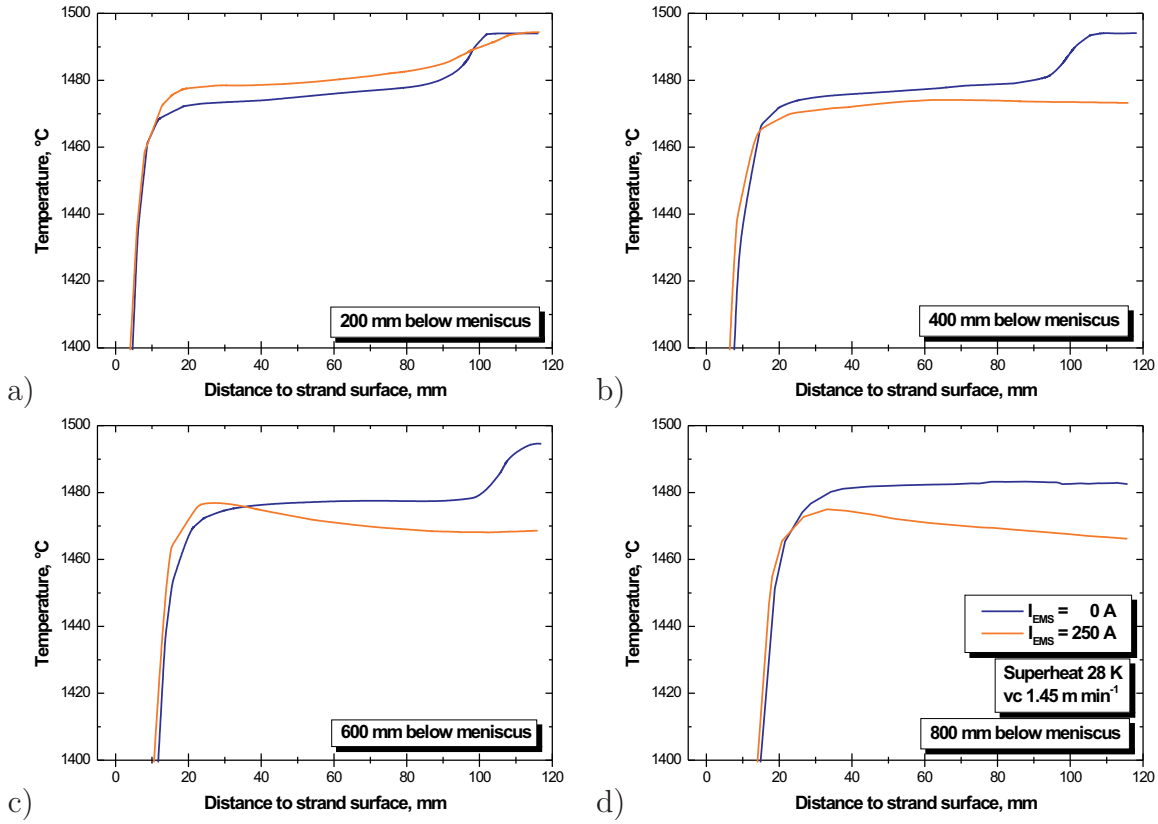

Figure 4-3.: *Temperature profile for different stirring currents* 0 *A (unstirred) and* 250 *A at different lengths below the meniscus: (a)* 200 *mm, (b)* 400 *mm, (c)* 600 *mm and (d)* 800 *mm.*

Defining the function $i_\kappa(z)$ as shown in **Fig. 4-4**, it is hence possible to tune the thermal conductivity of the liquid as,

$$\kappa_l(r,T,z) = \kappa_l(r,T,z) \cdot \left[1 + k_\kappa \cdot i_\kappa(z)\right] \tag{4-1}$$

where k_κ is a multiplicative factor. Evidently with this method the proposed method of simply increasing the thermal conductivity by a constant factor is amended by additionally considering the local strength of the stirrer. The characteristic of $i_\kappa(z)$ results directly from the velocity of the melt at the boundary to the mushy zone. In the present case the function has only been determined for a stirring current $I_{EMS} = 250\ A$, because this is the typical stirring current at the CC3. In case different stirring currents also were considered, the velocity distribution at the boundary would need to be evaluated again.

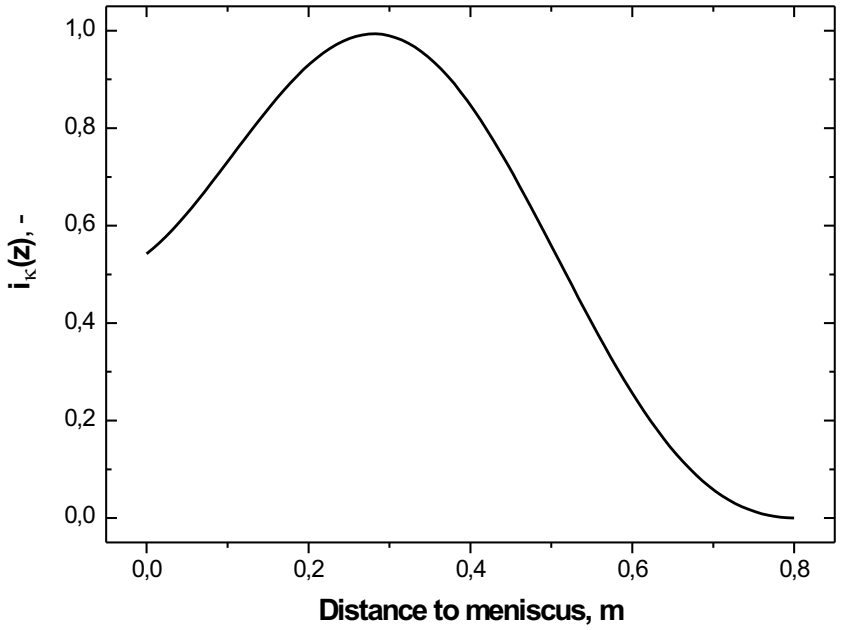

Figure 4-4.: *Function $i_\kappa(z)$.*

The factor k_κ could hence be determined through an iterative process of adjusting temperature profiles of the thermal model to the CALCOSOFT-3D simulations. Thereby the value of $k_\kappa = 3.0$ has proven to represent the conditions best, as can be seen in **Fig. 4-5**. This factor is in great consistency with the previously mentioned value from the literature, however with the difference that in the present case, the intensity of the stirrer was also considered. Although still showing slight differences of the profiles, the

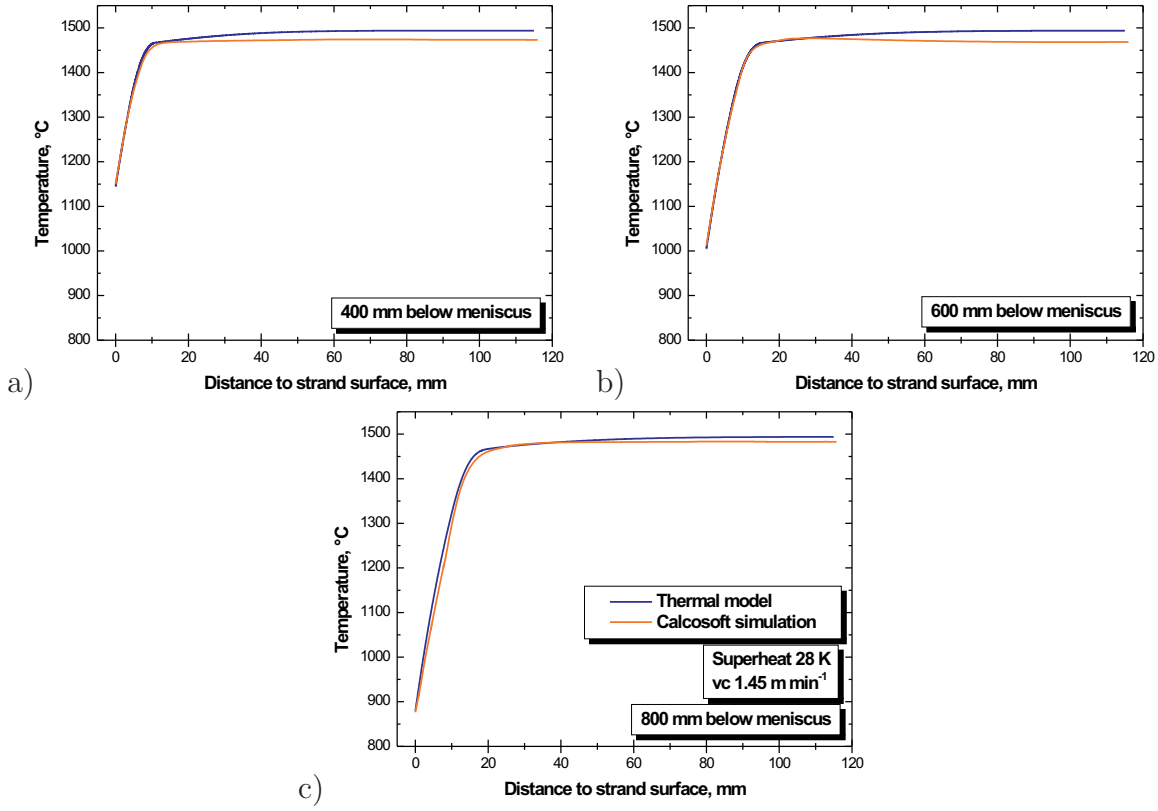

Figure 4-5.: *Temperature profiles for the adapted thermal model and* CALCOSOFT-3D *simulations at different lengths below the meniscus: (a)* 400 *mm, (b)* 600 *mm and (c)* 800 *mm.*

consistency is satisfactory, since the divergence most likely results from different mesh spacings: the complex 3D simulation only allows a limited number of nodes as compared to the thermal model, which permits extremely fine mesh spacings. The divergence of the profiles towards the centre of the strand is in the present case insignificant, since CET takes place at the mushy zone, not within the centre. Since similarity of the curves is given at temperatures around liquidus, discripancies towards the centre are irrelevant.

On the basis of this modification, the thermal model was hence prepared to feature an implementation of microstructure modelling according to the theoretical background presented in the previous section.

4.2. Numerical Microstructure Modelling

The practical realisation of the thermal model has been achieved using Borland Delphi Professional 7 provided by Borland Software Corporation. Delphi is the successor of the Turbo Pascal and has been chosen because of its manageability regarding user interfaces and database compatibility. The software product, which has been developed for modelling the CC3 at voestalpine Stahl Donawitz GmbH & Co. KG, is called SolMod 1.0 and features – amongst others – the determination of the temperature and fraction of solid distribution over the total strand length for the selected steel grade sb8x30n.

Within the frame of this program, the microstructural modelling was implemented as a subunit which receives all necessary data from the program overhead. These are:

- Mesh spacing over bloom radius,
- Mesh spacing over strand length,
- Temperature distribution,
- Fraction of solid distribution,
- Thermodynamic quantities for the steel grade (T_L, T_S, ...).

Since the thermal model underlies certain restrictions, several premises also apply to the microstructure model:

i. Assumption of axisymmetry – a 1d-slice is considered (however with varying thermal boundary conditions). This implies that only a radial differentiation of space and no segmental discretion is achieved. From a thermal viewpoint there is no distinction between fixed and loose side.

ii. Constant mesh spacing – The mesh spacing which is used for the macroscopic model is kept and no further subdivision of the mesh is performed for the cet-model. A

similar method is also applied by Thévoz [18]. Although other authors [20] recommand to use a finer mesh spacing for the microscopic model, the accuracy of the model is established by employing an extremely fine mesh spacing for the macroscopic model already.

iii. Uniformity of temperature distribution – the temperature is assumed constant within each mesh element. This results from the applied numeric scheme for the thermal model. The exact position of the dendrite tip is calulated by interpolating the temperature of the two adjacent nodes.

iv. Since the basis for the model is the temperature distribution solely, fluid dynamics are not considered. Hence melt-flow due to shrinkage or thermo-solutal buoyancy are not treated. Additionally diffusion processes are not taken into account actively. However the basic duffusion processes at the dendrite tip is allowed for according to the proposed ideas by Kurz and Fisher [11].

v. The presented model does not feature any method of multiphase modelling. The existence and formation of nuclei is based strictly on thermal considerations. The consideration of multiphase modelling has, for example, been conducted by Ludwig *et al.* [43].

vi. A coupling of the macroscopic model with the microscopic model is not implemented. The microstructure computation bases on the results of the thermal model. This procedure has also been proposed by Thévoz [24] and has mainly been adopted in order to speed up computation time.

4.2.1. General Procedure

The CET-model is a stepwise method which applies at every timestep t_k once a minimum number of 1 node has reached a fraction of solid $f_s = 1$. Hence the position of the liquidus isotherm is obtained from the given temperature field. Due to the mesh discretion, this position applies to a distinct node K_k where $T(r_k, t_k) = T_L$. The length of the undercooled zone dxt_k can then be determined using the model of Kurz and Fisher (section 3.2.1).

Subsequently, the undercooling of nodes inside this zone is computed on the basis of a simplified segregation model, as explained further on. In case dendrite fragmentation occurs (i. e. the strand is still inside or shortly below the mould), the amount of fragmented dendrites $N_{frag,k}$ is equally distributed over the nodes in the undercooled zone. Admittedly this may seem a rather arbitrary assumption – however seeing that $N_{frag,k}$ is afflicted with a fitting parameter anyway, the supposition is justifiable. Next to fragmentation, equiaxed crystallites are heterogeneously nucleated as a function of the node undercooling – their amount is described by the quantity $N_{het,k}$. The size of both types of crystallites is considered in the quantities $R_{frag,k}$ and $R_{het,k}$ respectively. In all subsequent timesteps these nuclei – originating both fragmentation and heterogenous nucleation – will grow according to the LGK-model (section 3.2.3) – again depending on the node undercooling. Next to transport mechanisms resulting from sinking, the nuclei are also transported downwards with the casting velocity. Hereby, it is assumed that the nuclei do not switch positions (i. e. node index).

With every subsequent timestep, the described phenomena occur again – at a different temperature distribution. Therefore, number and size of the nuclei vary from generation to generation. This implies that these quantities have to be considered generationwise from the very start to the final CET – resulting in a substantial memory usage.

Every timestep is finalized by determining the volume fraction of equiaxed crystallites f_e. In case f_e exceeds a given threshold it is assumed that CET occurs. For a better understanding the procedure sequence is illustrated in **Fig. A-5**; the necessary subroutine flowcharts are also displayed in appendix A. The details for calculating each necessary parameter are illustrated in the following.

4.2.2. Length of the Undercooled Zone

Generally, the length of the undercooled zone is given by the quotient of the undercooling at the dendrite tip ΔT and the gradient at the dendrite tip G:

$$dxt = \frac{\Delta T}{G} \tag{4-2}$$

From the complex model for the dendrite tip undercooling in section 3.2.1, a relation between the undercooling and the solidification velocity V can be established. Next to the parameters of **Tab. 3.I**, the parameters κ, ρ and c_p at liquidus temperature are required. Since these values are composition dependant, their amounts at $T = T_L$ have to be determined by the already mentioned thermodynamic database. The exact values can be found in the appendix in **Tab. C.II**. In order to speed up computation time a function for $\Delta T(V)$ has been found. This dependency – illustrated in **Fig. 4-6** – is best approximated by the following equation,

$$\Delta T(V) = 0.03299 - 22.64 \cdot \sqrt{V} \cdot \ln V \tag{4-3}$$

yielding a correlation factor higher than 99 %. The figure also shows values published by Etienne [21], who has adopted a similar method for calculating the dendrite tip undercooling.

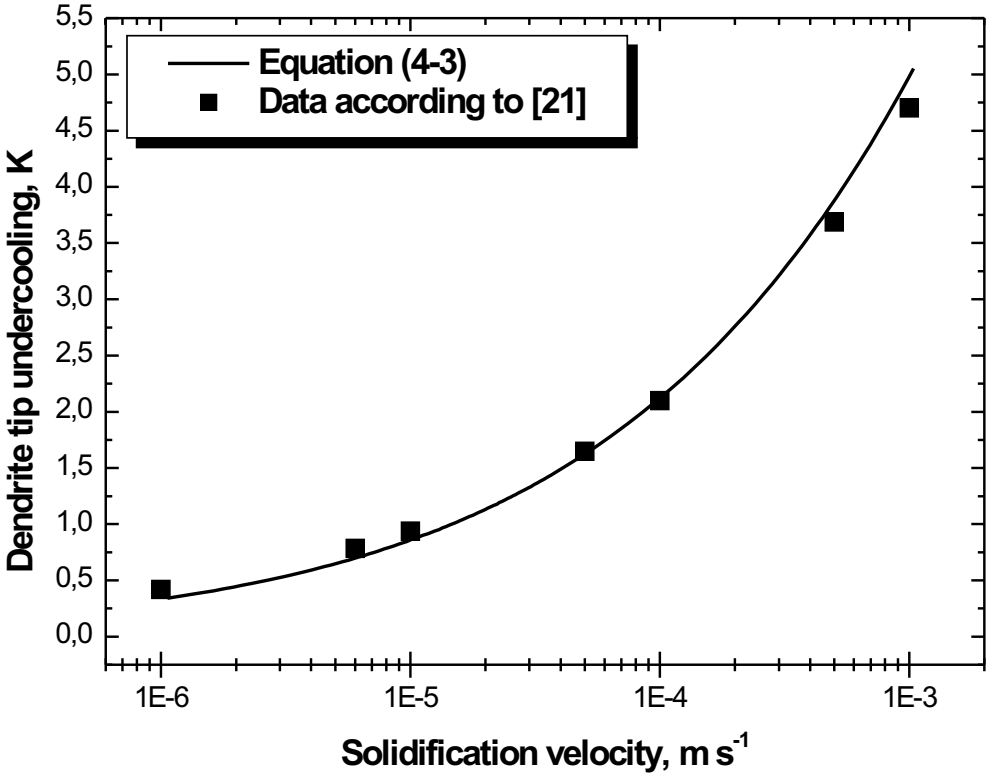

Figure 4-6.: *Dendrite tip undercooling as a function of solidification velocity.*

4.2.3. Amount of Undercooling

In order to consider segregation effects, which strongly influence the undercooling, a simplified proposed by Etienne [21] has been applied. It is assumed that nodes which do not contain solid fraction, are at the starting composition C_O. Hence, as soon as equiaxed fraction is present, the composition of the liquid C_L increases and reaches the liquidus value C_{Liq} once the remaining volume is at a certain limit. Therefore,

$$C_L = C_{Liq} \quad \text{if} \quad f_e = F_{seg} \tag{4-4}$$

is valid with F_{seg} as a upper limit. Before reaching this limit the liquid's composition is given by:

$$C_L = C_0 + \frac{f_e}{F_{seg}} \cdot (C_{Liq} - C_0) \tag{4-5}$$

The idea behind this model is illustrated in **Fig. 4-7**. It can be seen from the figure that, in case no segregation is present, the undercooling ΔT equals the global undercooling ΔT_G which is the undercooling at the intial composition: $\Delta T_G = T_L - T$. However, as soon as $C_L \neq C_0$ the local undercooling decreases, eventually reaching zero once equaling the liquidus concentration.

4.2.4. Fragmentation

It has been explained in section 3.2.2.1 that fragmentation only occurs if the defined fragmentation criterion $C_R > 1$ is fulfilled. Naturally, dendrite fragmentation will only be considered if the melt is agitated by the stirrer.

It has been shown that the amount of fragmented dendrites is inversely proportional to the microstructural parameters λ_1 and λ_2 [7]:

$$N_{frag} \sim n_f = \frac{4}{\lambda_1^2 \cdot \lambda_2} \tag{4-6}$$

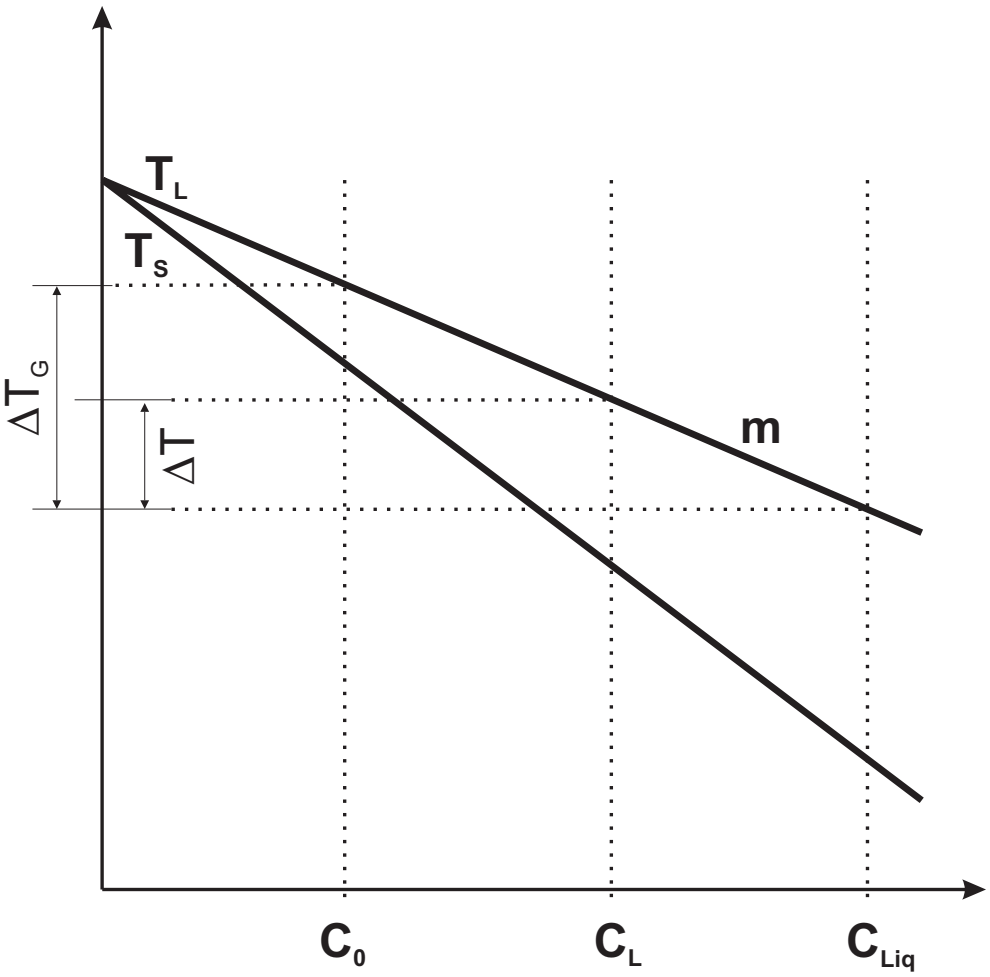

Figure 4-7.: *Simple model for considering the enrichment of the melt ΔT_G is the gobal undercooling, ΔT the local undercooling.*

The parameters λ_1 and λ_2 are determined according to formulae from the literature [35, 44]:

$$\lambda_1 = 0.67 \times 10^{-4} \cdot \dot{T}^{-0.424} \tag{4-7}$$

$$\lambda_2 = (21.52764 - 9.4 \cdot C_0) \cdot \dot{T}^{0.4+0.08 \cdot C_0} \times 10^{-6} \tag{4-8}$$

Moreover, the amount of fragmented dendrites depends on their constitution, respectively the length which can be hit by stirred liquid. In this context, Ayata *et al.* [7] have

reported that the maximum fraction of solid at which the mushy zone can be stirred, $f_{s,max}$, is a function of the stirring velocity $\vec{u}$ and the carbon content C_0:

$$f_{s,max} = \frac{\left(3.93 \cdot C_0^2 - 6.19 \cdot C_0 + 3.75\right)}{1-k} \times 10^{-2} \cdot \left[(|\vec{u}| - 0.09) \cdot 100\right]^{0.6} \tag{4-9}$$

In the present case, the stirring velocity $\vec{u}$ is deduced from the simulations described in section 4.1 – its characteristic is similar to that of **Fig. 4-4**. The according length of the mushy zone is however decreased by the length of $8 \cdot \lambda_2$, since it is assumed that below that length only remelting of the dendrite arms occurs, since they are not enough developed. (cf. section 2.1.1). Therefore the overall fragmented length l_{frag} equals:

$$l_{frag} = r_{f_s=0} - r_{f_s=f_{s,max}} - 8 \cdot \lambda_2 \tag{4-10}$$

In case l_{frag} is smaller than zero, no fragmentation will occur; if $l_{frag} > 0$ the total density of nuclei N_{frag} is regulated accordingly. Lastly, it is assumed that the fraction of fragmented dendrites which are actually transported into the undercooled zone is equally spread over the number nodes of the zone N_T:

$$N_{frag,k} = F_{frag,no} \cdot n_f \cdot \frac{l_{frag}}{dxt} \cdot \frac{1}{N_T} \tag{4-11}$$

As the size of the nuclei is hard to measure, no assured values can be found in the literature. In the present case, they are assumed to have a constant size at the timestep of fragmentation which is given by the fitting parameter $F_{frag,rad}$.

4.2.5. Heterogenous Nucleation

The GAUSSian approach to the law for heterogenous nucleation can be adopted instantly, since the three necessary parameters ΔT_N, ΔT_σ and n_{max} need to be determined experimentally anyway.

Clearly the change in grain density for heterogenous nucleation at a given timestep $N_{het,k}$ results from the difference of the grain densities between the undercoolings ΔT_k and ΔT_{k-1}:

$$N_{het,k} = \int_{\Delta T'=\Delta T_{k-1}}^{\Delta T'=\Delta T_k} \frac{\mathrm{d}n_{het}}{\mathrm{d}\Delta T} \cdot \mathrm{d}\Delta T' \tag{4-12}$$

In the model the necessary critical radius for nucleation is not calculated. It its therefore assumed that the radius of the nuclei equals zero. Seeing that a fitting factor has been introduced anyway, nuclei which would not reach the critical radius do not need to be considered.

4.2.6. Growth of Nuclei

Obviously, the theoretical basis for calculating the growth velocity V_e of the equiaxed dendrites as a function of the undercooling, is alike that for calculating the length of the undercooled zone as a function of the growth velocity of the columnar zone (cf. section 4.2.2). However, since equiaxed growth is not only influenced by the chemical undercooling ΔT_C, and the curvature undercooling ΔT_R, but also by the thermal undercooling ΔT_T, the approach is slightly different.

The necessary data for calculating $V_e(\Delta T)$ are shown in **Tab. 3.I** and **C.II**. Applying these values and combining equations **(3-27)**-**(3-30)**, yields the function $V_e(\Delta T)$, which describes the growth of the equiaxed nuclei as a function of the undercooling:

$$V_e(\Delta T) = 5.86 \times 10^{-3}\Delta T^3 + 8.16 \times 10^{-3}\Delta T^2 - 7.13 \times 10^{-7}\Delta T + 9.43 \times 10^{-9} \tag{4-13}$$

The characteristic of this function is shown in **Fig. 4-8**, together with values published by Etienne [21]. On the basis of this dependency the growth of the nuclei at every timestep is given by:

$$\Delta R_e = V_e \cdot \Delta t \tag{4-14}$$

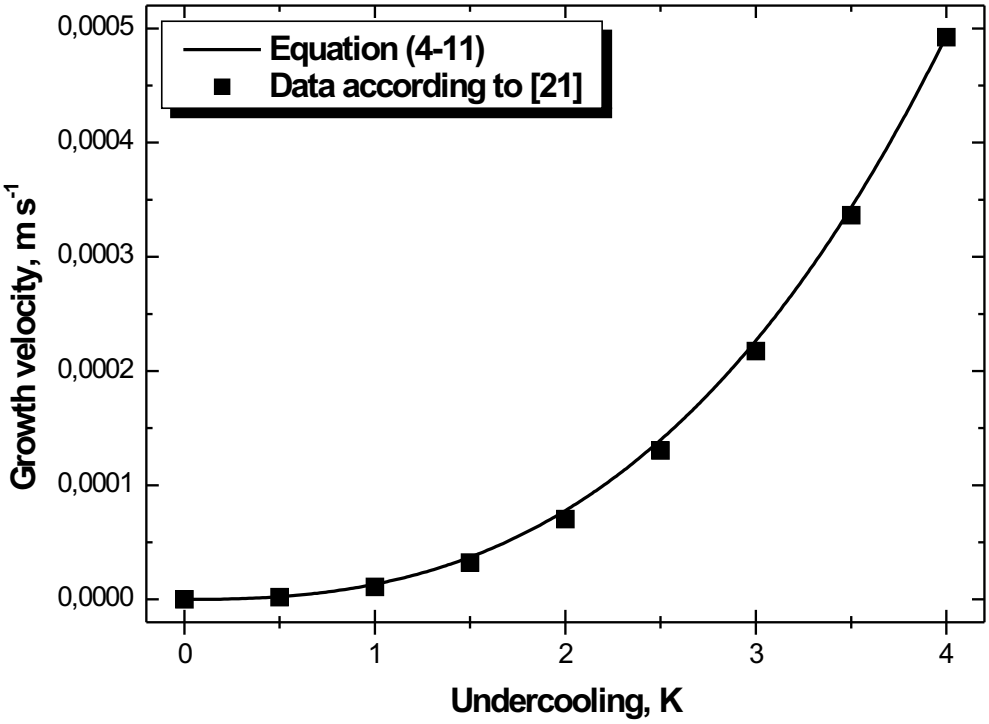

Figure 4-8.: *Equiaxed growth velocity as a function of undercooling.*

4.2.7. Transportation

As aforehand mentioned, the transportation of the nuclei is composed of two superimposing mechanisms: On the one hand, the nuclei are transported with the strand due to the casting velocity – whilst constant in magnitude (provided the strand is cast at constant speed), the vector alters its orientation over the length of the strand.

The angle of orientation γ is described by

$$\gamma = \frac{l(t)}{R_S} \tag{4-15}$$

where $l(t)$ is the distance to the meniscus and R_S is the total radius of the strand – a plant parameter. On the other hand, the nuclei are moved downwards perpendicularly by gravitation. Although this vector is constant in its orientation – always strictly downwards – it changes in magnitude due to the growth of the particles. STOKES' law, which applies to such a phenomenon of sinking particles in a liquid, has been described in section 3.2.4.

The differences in the effects of these transportation mechanisms on the nuclei density of the fixed and loose side, require a separate treatment of the two cases.

4.2.7.1. Fixed Side

On the fixed side it can be assumed that the nuclei will be transported towards the columnar front, where they will either be rejected and remain in the undercooled zone, or get caught by the dendrites. In case large enough, equiaxed crystallites are caught, and other sedimenting ones will accumulate on the first crystallite and form the illustrated sedimented pile (**Fig. 3-4**). Since the catching of the nuclei cannot be simulated with the presented methods, it has to be assumed that the nuclei will accrue before the columnar solidification front. Evidently this process decreases the number of nuclei in the remaining nodes of the undercooled zone. Since an absolute physical quantification of the amount of crystallites which amass before the columnar front cannot be given, the introduction of a fitting factor is again required. Moreover since sedimentation also affects the nuclei which can be found more towards the liquidus isotherm, the number of nuclei has to be altered for each node in the undercooled zone. Hence the change in the number of nuclei ΔN for a given node j can be calculated by

$$\Delta N_{j,k} = N_{j-1,k} \cdot F_{trans,fs} \cdot f_{sed} \cdot \frac{\Delta l}{\Delta r} \tag{4-16}$$

where $F_{trans,fs}$ is the fitting factor for sedimentation on the fixed side. f_{sed} is the proposed ratio (cf. section 3.2.4) which is a function of the nuclei size and γ. The necessary material data are given in the appendix C. Δl and Δr are the longitudinal and the radial mesh spacing respectively. This ratio results from the consideration that nuclei will not switch nodes, unless the time necessary for the movement with the strand is smaller than that for downward sinking (the product of the last two components in equation **(4-16)** is a ratio of time). Lastly, the amount of nuclei in the node $j-1$ has to decrease according to the increase in its neighboured node j.

4.2.7.2. Loose Side

With regard to the movement of the particles on the loose side, most of the ideas presented for the fixed side also apply. However the justification for the use of a fitting factor is slightly different: STOKES' law assumes that the particles are spherical – a strong contradiction the to the form of equiaxed crystallites typically developing sidearms. Therefore, their sinking velocity will be substantially smaller than the actually predicted one – this inhibition of sinking is therefore reproduced by the fitting factor $F_{trans,ls}$.

Another difference to the fixed side is that in this case only the node immediately in front of the columnar front needs to be considered. Only the nuclei in this node could possibly evoke a CET. Consequently, it is irrelevant where the sinking nuclei go to – once they have left the node they are lost and cannot contribute to the CET. Subsequently the calculation algorithm is simpler and only one node ($j = 0$) needs consideration:

$$\Delta N_{0,k} = -F_{trans,ls} \cdot f_{sed} \cdot \frac{\Delta l}{\Delta r} \tag{4-17}$$

Hence equation **(4-17)** yields the decrease of nuclei density in the node ahead the columnar front for each timestep k.

4.2.8. Transition

Although it is assumed that the nuclei do not move freely within the mushy zone, still all nuclei will contribute to the CET. Therefore the fraction of equiaxed crystallites needs to be determined in all nodes. Moreover, all generations of nuclei need consideration since it is assumed that the nuclei are at least transported with the speed of the strand. This means that nuclei which have been generated several timesteps before the actual CET also play a role.

Ultimately the fraction of equiaxed nuclei f_e at a given timestep K can be determined by

$$f_{e,K} = \frac{4}{3} \cdot \pi \cdot V_n \cdot \sum_{k=0}^{K} \sum_{j=0}^{N_T} \left(N_{het,j,k} \cdot R_{het,j,k}^3 + N_{frag,j,k} \cdot R_{frag,j,k}^3 \right) \tag{4-18}$$

where V_n is the volume size of the considered mesh element.

$$V_n = 1 \cdot \Delta l \cdot \Delta r \tag{4-19}$$

The factor 1 results from the quasi-1D treatment of the problem, wherefore the thickness of the mesh elements is always equal one.

Once the fraction of equiaxed nuclei has exceeded a given threshold F_{CET} as a fitting parameter, CET occurs and the procedure stops running – the objective of the computation is accomplished.

5. Numerical and Practical Results

Parallel to the development of the proposed CET-model, plant trials were carried out at the CC3 at voestalpine Stahl Donawitz GmbH & Co. KG. In these experiments the steelgrade SB8X30N was cast under different casting conditions with variations of

- superheat,
- casting velocity,
- stirring current for the mould electromagnetic stirrer,
- stirring current for the final electromagnetic stirrer.

In normal casting practice, the stirring current of both stirrers is generally not varied. Therefore the latter two variations are only of minor interest to the present subject, the first two are highly important for this analysis.

In order to determine the CET on the cast blooms, cylindrical discs were cut off directly from the semi-finished product. Hence rectangular slices were sawn out of the discs, ground, polished and etched with picric acid in order to make the primary solidification structure visible.

Thereafter the CET was determined by optical inspection under the microscope. However, the exact position of the CET cannot be ascertained with absolute reliability, since the CET is actually a transition zone within which columnar growth is increasingly inhibited while equiaxed solidification begins to dominate. From the photograph of one of the specimen in **Fig. 5-1**, it can evidently be seen that no definite point exists for the CET. The probable position is marked in **Fig. 5-2**.

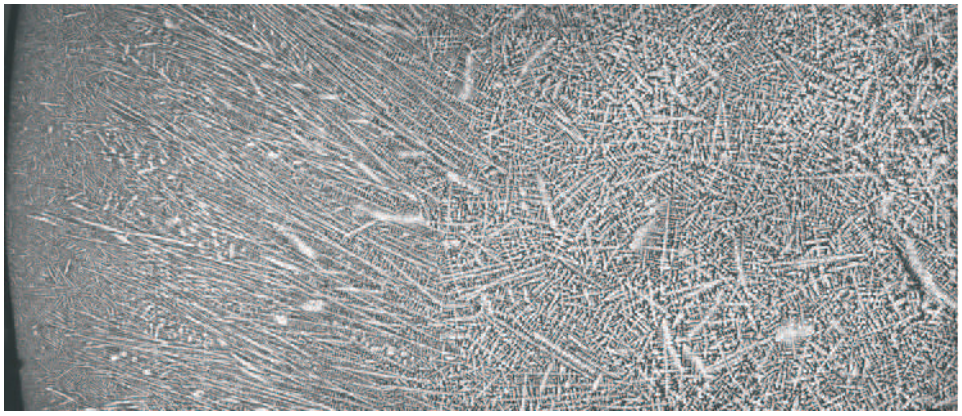

Figure 5-1.: *Etched specimen – the transition zone between columnar and equiaxed solidification is clearly visible.*

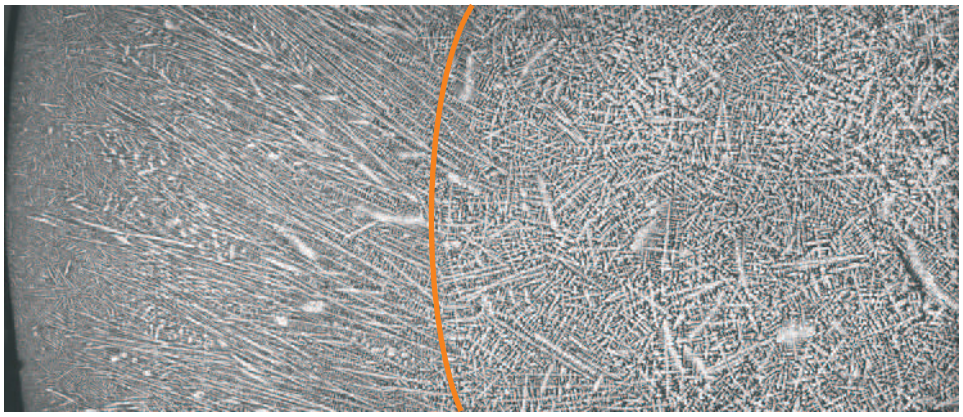

Figure 5-2.: *Etched specimen – supposed point of transition.*

5.1. Determination of the Ratio of Equiaxed Solidification

In the context of equiaxed solidification, the amount of area of equiaxed solidification is frequently an interesting quantity. Seeing that the transition occurs at different positions for the fixed and the loose side of the strand, the calculation of this measure is not straightforward.

In the present study, it is assumed that the enclosed area with the equiaxed nuclei is composed of two semi-circles with radii R_F and R_L respectively as shown in **Fig. 5-3**.

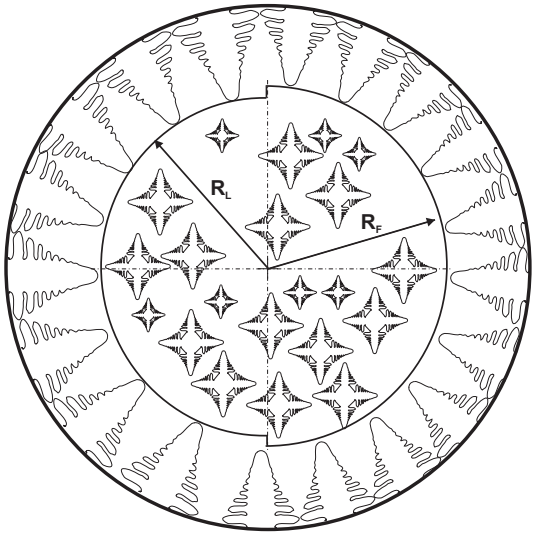

Figure 5-3.: *Schematic illustration of the determination of the area of equiaxed solidification.*

The percentage of area of equiaxed solidification is hence given by,

$$\%equi_{sol} = \frac{R_F^2 + R_L^2}{2 \cdot R_S^2} \tag{5-1}$$

where R_S is the total radius of the strand.

5.2. Practical Results

5.2.1. Variation of Superheat

Only a limited number of results was utilized for the evaluation of the CET. These were results of experiments where typical casting conditions were prevailing: no starting batch, normal level of stirring current for both stirrers and constant casting speed. All batches were cast with a casting velocity of $v_c = 1.45\ m\,min^{-1}$.

The necessary casting parameters and the resulting positions of CET are given in **Tab. 5.I**. The graphical illustration of these results can be found in **Fig. 5-4**. The figure clearly shows that CET occurs later on the loose side of the strand for the described reasons.

Table 5.I.: *Casting parameters and position of* CET *for plant trials at the CC3.*

Superheat	I_{ems}	CET shell thickness	
$[K]$	$[A]$	Loose side	Fixed side
		$[mm]$	$[mm]$
24	250	31	25
26	250	29	28
29	250	34	24
30	250	29	27
30	250	32	28
30	250	38	32
30	250	37	33
30	250	35	31
31	250	36	32
36	250	31	29
38	249	52	38
39	250	33	29
41	243	52	34
41	249	55	33
46	250	35	27
51	250	35	28
52	250	44	28
53	250	45	26

Moreover, CET is retarded with increasing superheat. This behaviour is especially distinct on the fixed side. On the loose side the impact is not as strong, however a certain retardation can also be observed, once the superheat has reached a critical value. This behaviour has also been observed by Lesoult [6] (cf. **Fig. 2-9**). Obviously the sedimentation effects on the fixed side are influential enough as to still prevent the columnar front from growing further.

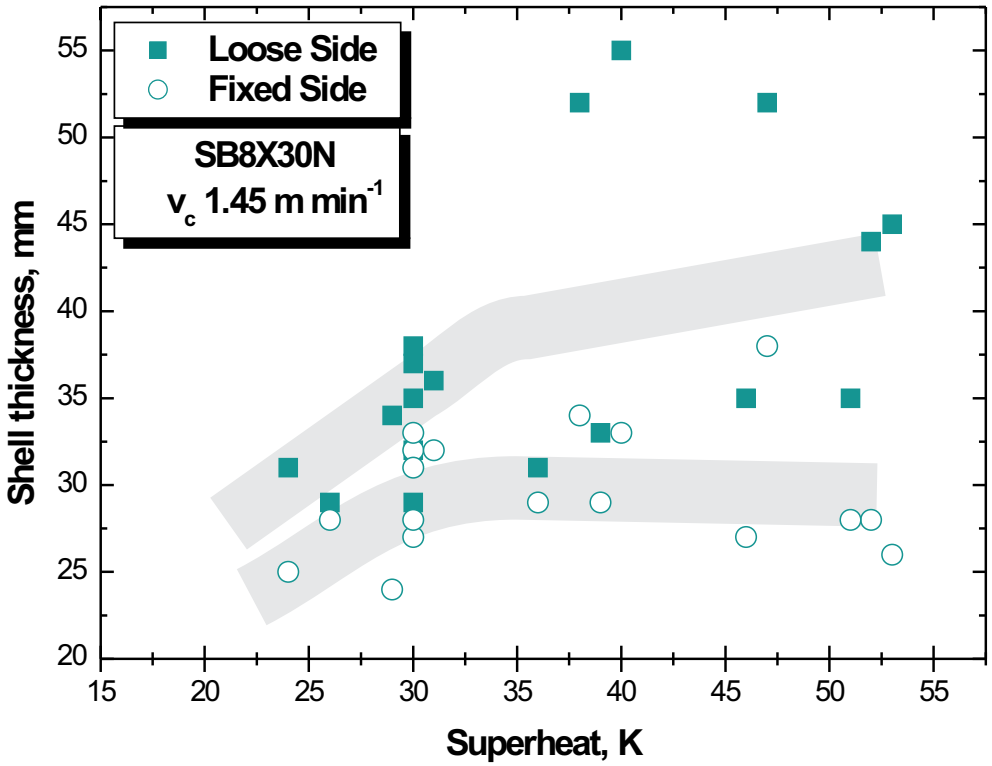

Figure 5-4.: *Strand shell thickness at which* CET *occurs as a function of the melt superheat for fixed and loose side – practical results.*

5.2.2. Variation of Casting Velocity

Next to a variation of superheat, a few plant trials were conducted where the casting velocity was altered within the technical possibilities. The superheat of the melt can be assumed constant for all trials. Unfortunately only one specimen was obtained for each of the casting velocities. Therefore the range and reliability of the results is limited.

Trials were carried out for casting velocities of 1.40, 1.45, 1.50 and 1.55 $m\,min^{-1}$. The according positions of the CET are illustrated in **Fig. 5-5**. These results show a clear retardation of the CET with rising casting velocity – a trend which could possibly be explained by a shorter period of stirring. However, the heat withdrawal in the mould increases with the casting velocity – this would in turn promote CET. Therefore, no clear prognosis of the influence of the casting speed can be given at first sight. An increasing amount of plant trials is necessary for a clear prediction of the influence.

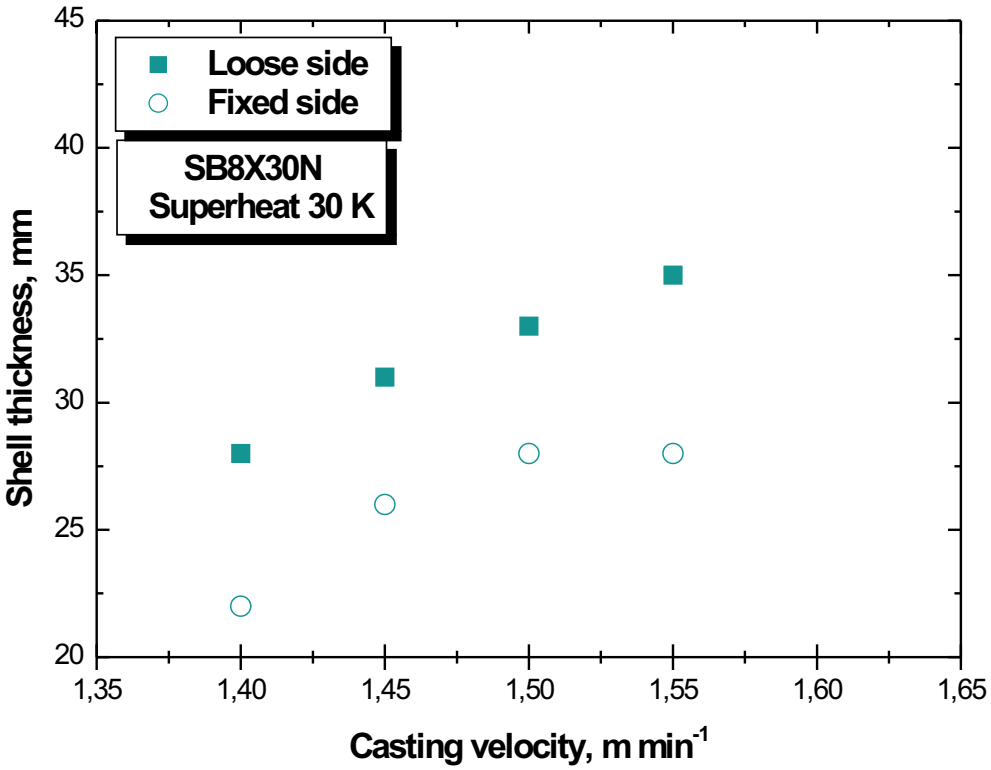

Figure 5-5.: *Strand shell thickness at which* CET *occurs as a function of the casting speed for fixed and loose side – practical results.*

Seeing that only one value is available for each casting speed, the results have to be regarded with great caution.

5.3. Numerical Results

5.3.1. Variation of Superheat

Since the described model requires the definition of several fitting parameters, the practical experiments were partly used as a basis for their estimation. In a time consuming iterative process the results of the model were tuned to represent the experimental ones for a selected superheat. Seeing that several plant trials were conducted for a superheat of app. 30 K, the fitting parameters were at first defined to meet the results of these seven experiments.

On this basis, numerical results were obtained for several superheats and the fitting parameters adjusted accordingly. In view of the fact that all results represent the practically estimated trend, the model can be used to predict the influence of the superheat on the CET for this chosen caster.

The results of the CET-model shown in **Fig. 5-6** were calculated with the fitting parameters shown in **Tab. 5.II**, together with values which have been proposed by Etienne [21] for a 0.75 %-C steel. However, since Etienne has not explicitly considered fragmentation, no values can be provided for comparison. Evidently most of the parameters match very well, the only considerable difference is the value of n_{max}. In the publication [21], it is indicated that the value of $1.5 \times 10^{16}\ m^{-3}$ seems exceedingly high. In the present model, the value of $3.5 \times 10^{11}\ m^{-3}$ seems more likely.

The results in **Fig. 5-6** show a satisfactory consistency with those of the plant trials. Again, the difference between fixed and loose side is obvious. Furthermore, the change of the position of the CET with superheat is well reflected by the model – including a limit for the CET at high superheats, as explained in the previous section. It is interesting to note that the model confirms the previously mentioned assumption, of a retardation of the CET on the fixed side.

5.3.2. Variation of Casting Velocity

Since the model features a wider variation of the casting velocity than the caster does, the CET-behaviour was analysed for numerous casting velocities. From the results in **Fig. 5-7** it can be seen that the clear trend of the practical experiments cannot be fully reproduced by the model. In the range of the usual casting velocities of this steel grade ($1.45\ m\,min^{-1}$), the reproduction of the model is satisfying. However, casting velocities outside this range cannot be mirrored that well, since the mould heat flux changes with casting velocity. Seeing that the presented simulations were all carried out for a constant mould heat flux – laking the necessary practical data – no clear prediction on the influence of the casting speed can presently be done.

Table 5.II.: *Fitting parameters for the* CET*-model.*

	Obtained fitting parameters	Values according to Etienne [21]
ΔT_N	6.5 K	6.5 K
ΔT_σ	0.8 K	0.8 K
n_{max}	3.5×10^{11} m^{-3}	1.5×10^{16} m^{-3}
$F_{frag,no}$	0.5	–
$F_{frag,rad}$	5×10^{-5} m	–
F_{CET}	0.68	0.74
$F_{trans,ls}$	1.5×10^{-7}	–
$F_{trans,fs}$	1.5×10^{-7}	–
F_{seg}	0.69	0.77

5.3.3. Effect of Electromagnetic Stirring

In a last series of simulations, the effect of mould electromagnetic stirring on the CET was analysed. Hereby the two extrema – no stirring, and stirring with full intensity ($I_{EMS} = 250$ A) – were taken as a basis for the simulations. From the literature study it is evident that in absence of electromagnetic stirring the CET should – if at all – occur significantly later. The model mirrors the expected behaviour very well, as can be seen in **Fig. 5-8** and **Fig. 5-9**. The two figures show the shift of the CET at the fixed and the loose side for various superheats for stirred and unstirred melts. At higher superheats, no CET will occur at the loose side – a dependency which the practical experiments have also shown. The diagrams indicate the positions of the strand centre at 115 mm – since the CET occurs nearly in the centre, the structure of the unstirred bloom is assumed to be almost fully columnar.

5.4. Comparison

In order to effectively compare the results of the practical experiments to the model's output, the percentage of area of equiaxed solidification is taken as a measure. The corresponding graphs can be found in **Fig. 5-10** and **Fig. 5-11**. As it can be expected the results show great conformity for a variation of superheat – again an absolute limit of the area of equiaxed solidification at high superheats is interesting to note.

Regarding a change in casting velocity, the clear trend of the plant trials cannot be reproduced by the numeric model for low casting speeds. Once again it has to be stated that the experimental values base on very few measurements wherefore their reasonability is questionable. Moreover the thermal boundary conditions for changing casting velocities differ significantly. Since no practical data was available for that case, an exact reproduction of the practical results is presently not possible. Nonetheless the model shows a certain conformity for the casting velocities 1.45, 1.50 and 1.55 $m\,min^{-1}$.

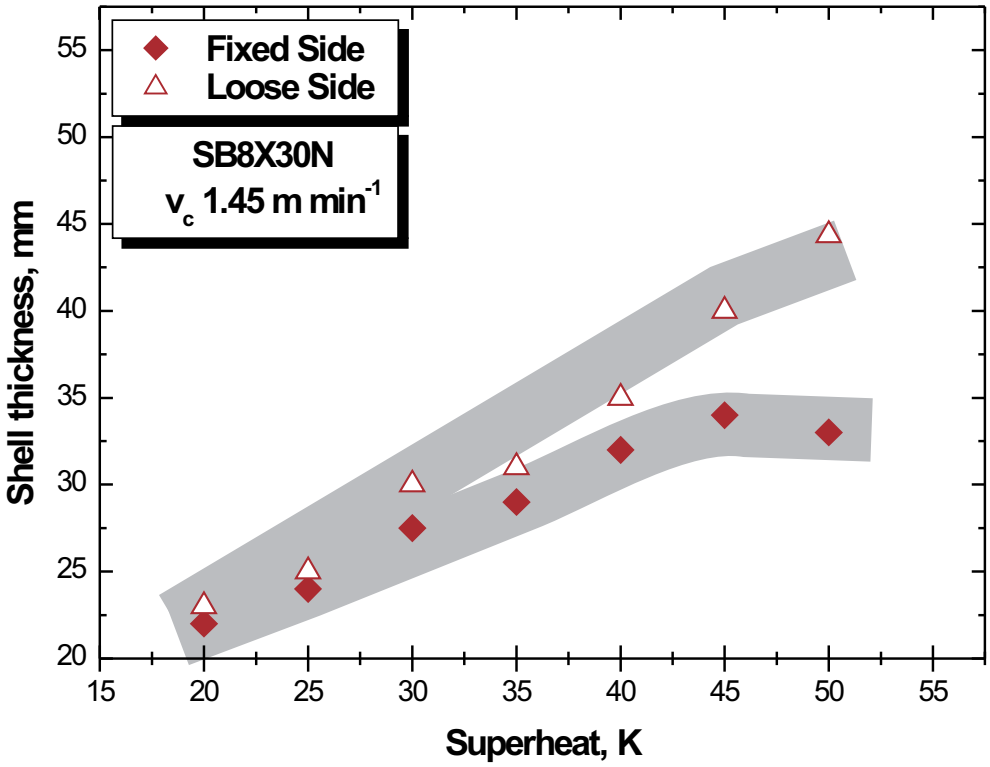

Figure 5-6.: *Strand shell thickness at which* CET *occurs as a function of the melt superheat for fixed and loose side – calculated results.*

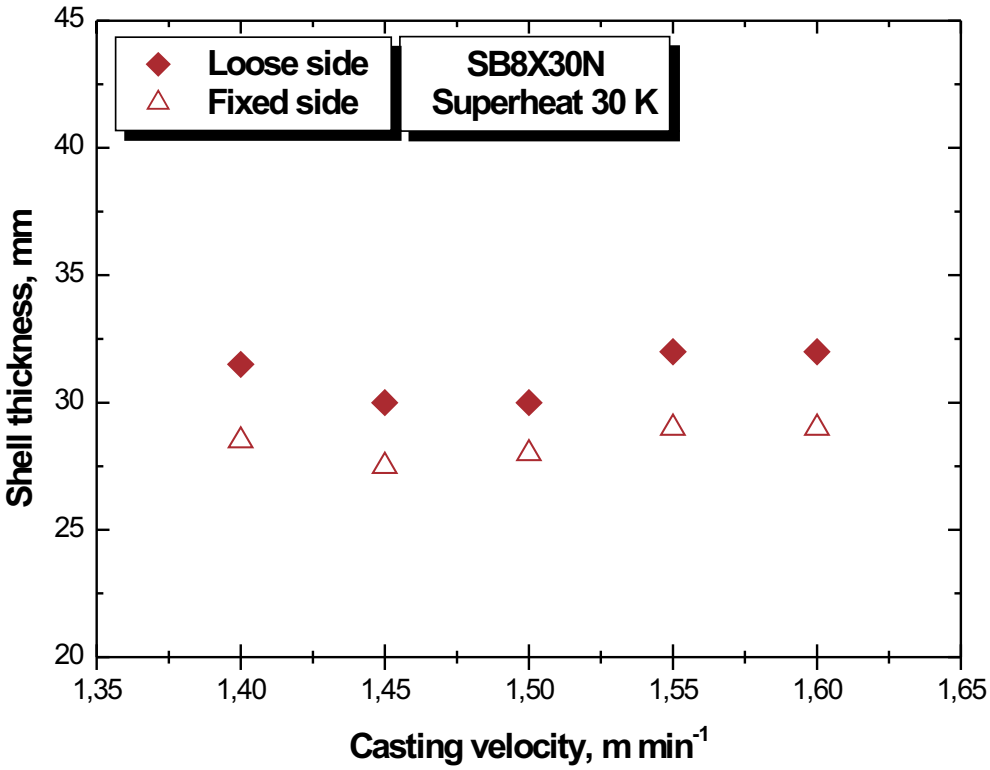

Figure 5-7.: *Strand shell thickness at which* CET *occurs as a function of the casting speed for fixed and loose side – calculated results.*

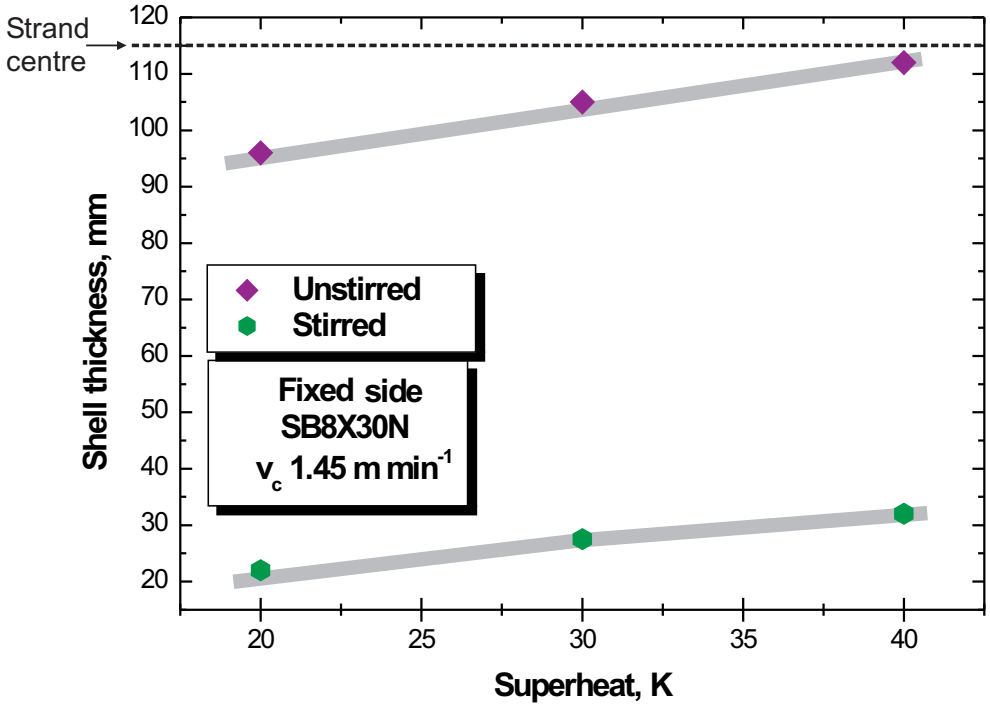

Figure 5-8.: *Strand shell thickness at which* CET *occurs as a function of superheat for stirred and unstirred melts at the fixed side.*

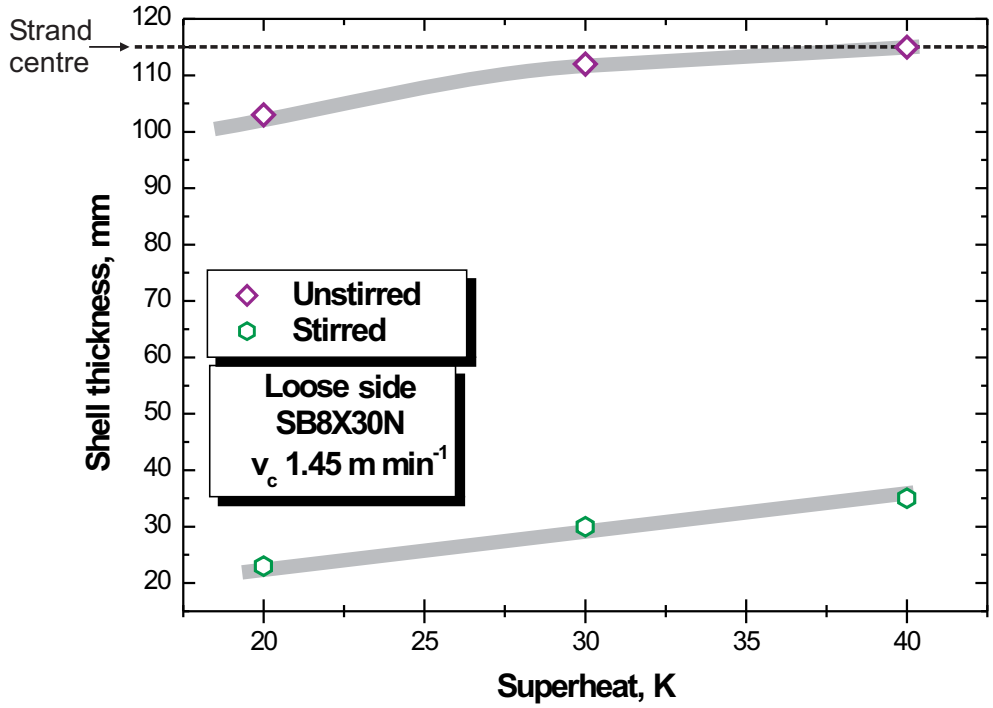

Figure 5-9.: *Strand shell thickness at which* CET *occurs as a function of superheat for stirred and unstirred melts at the loose side.*

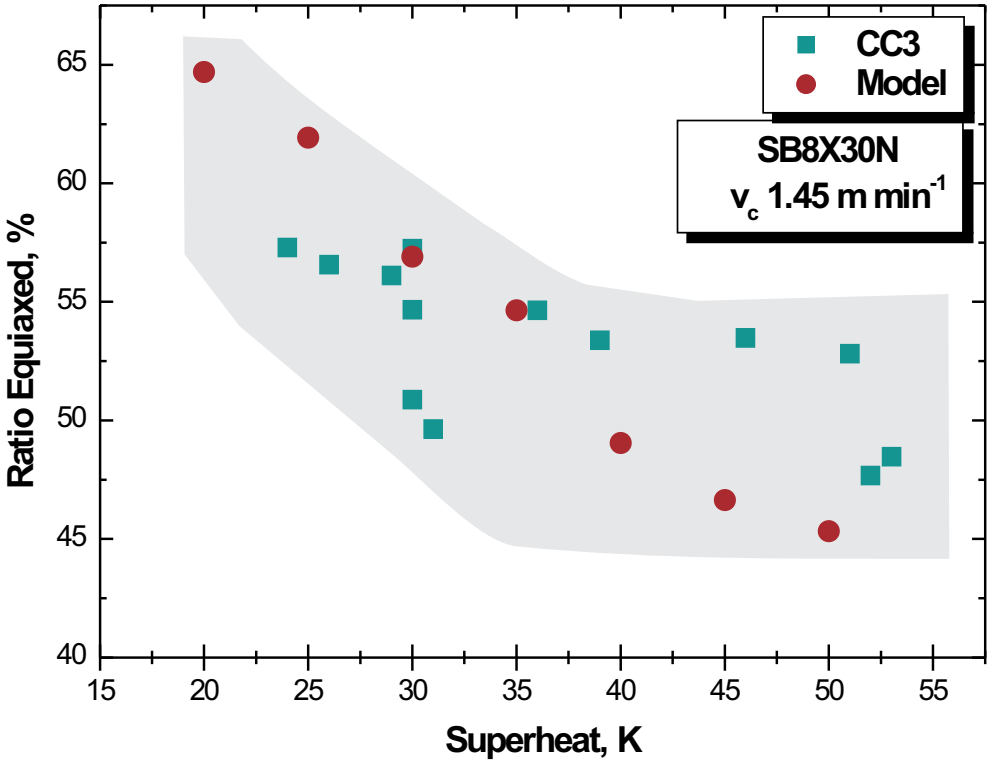

Figure 5-10.: *Ratio of equiaxed solidification as a function of the melt superheat.*

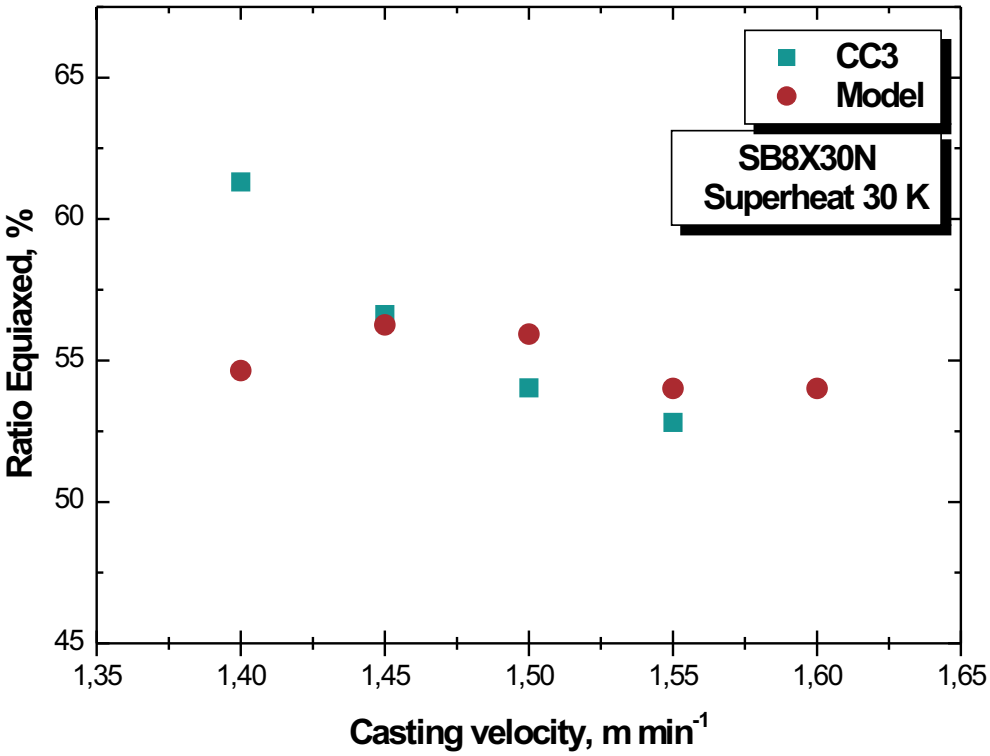

Figure 5-11.: *Ratio of equiaxed solidification as a function of casting velocity.*

6. Conclusion

In the present work, the CET during the continuous casting of steel has been treated. In has been shown that an equiaxed solidification is very useful when casting blooms or billets, since it minimises the level of macro segregations. These macro segregations are especially harmful for high carbon steels, where they lead to the formation of cementite networks which cannot be removed in subsequent process steps. Accordingly, a maximisation of the amount of equiaxed solidification is an important issue during the process.

It is commonly known that two possibilities of attaining an earlier CET exist: The application of electromagnetic stirring has the effect that the thermal gradient within the liquid is flattened, leading to an increased heat removal. Moreover, the agitated melt is transported into the mushy zone, and remelts secondary dendrite arms which are then available as equiaxed crystallites. This effect is generally known as fragmentation. Secondly, an equiaxed solidification is promoted by decreasing the steel superheat, since this facilitates the formation of an undercooled zone – a necessity for equiaxed solidification.

The aim of this work was to compile a numeric model for analysing the possibilities of influencing the columnar to equiaxed transition. In the first part of this work the necessary theoretical basics for such a model are presented. Generally it can be assumed that such a transition occurs once a sufficient number of equiaxed nuclei exist for blocking the columnar front. The existence of these nuclei must be in the undercooled zone ahead of the dendrites. It was shown that this zone can be computed by appropriate models which are published in the literature. Furthermore two mechanisms which lead to the existence of such nuclei were regarded. Nuclei can either originate the fragmentation of the secondary dendrite arms from the columnar front or can heterogeneously be nucleated

in the undercooled zone. The necessary dependencies have been illustrated. Since the nuclei will also grow in the undercooled zone, their growth as a function of temperature also needs to be considered. This has been achieved by the application of the LGK-model. Lastly, the nuclei can increasingly be transported once they have reached sizes at which gravitation starts to play a role. Since this possibly leads to an increase of the nuclei density ahead of the columnar front, an approach to quantifying this phenomenon is presented.

Based upon an existing thermal model of the continuous casting machine CC3 at voestalpine Stahl Donawitz GmbH & Co. KG the presented basics have been implemented for examining the CET at this caster. This independent software was developed at the *CD-Laboratory for Metallurgical Fundamentals of Continuous Casting Processes* on the basis of the programming language DELPHI. The steps for such work have been illustrated. Since the presented model requires the definition of several fitting parameters, which could only be determined experimentally, plant trials with changing casting speed and superheat were parallelly conducted at the caster. Since these trials were only conducted for a specific steel grade, the validity of the model is accordingly limited.

The plant observations show that a considerable difference for the CET exists between the fixed and the loose side of the strand. This is attributed to the fact that the nuclei accumulate or disperse ahead of the columnar front respectively, due to the explained sinking effects. Moreover, the experiments demonstrate that lower superheats shift the CET to shorter times. Higher superheats postpone the CET. When regarding very high superheats, it is observed that the CET is not held back further, especially at the fixed side. This observation – which has also been confirmed by literature results – is attributed to the fact that sedimentation effects outweigh the influence of the superheat and promote the possibility of a transition. With regard to a variation of casting velocity, a very limited database was available for analysing this influence. The practical experiments show that a rising casting speed leads to considerably later transitions.

The implemented model represents the trend of a later transition with rising superheat very well. Moreover the described effect of constant transitions with very high superheats

is also reflected by the model. However, the effect of a retarded transition with rising casting speeds cannot be fully emulated by the model. Furthermore, the model clearly demonstrates the differences of the CET between fixed and loose side.

Within the range of the casting speeds which are technically possible at the caster, the model reproduces the practical experiments acceptably well. With casting velocities outside this range, the model cannot mirror the practical results precisely. This could however be due to the fact that the heat flux in the mould changes substantially with casting speed – a fact which could not be reflected by the model, laking the appropriate practical data. Lastly, simulations have shown that most of the strand cross section solidifies columnarly in absence of electromagnetic stirring. These observations are also confirmed by plant trials which show a completely columnar solidification of the strand if no stirring is applied.

Admittedly the presented model requires the definition of several fitting parameters, since a full coupling of the CET-model with the thermal model was not the aim of this thesis. Several simplifications had to be taken in order to make the realisation within the given frame possible. However the achievement of a more sophisticated model (e. g. multiphase) would have gone beyond the scope of this project.

Finally, it can be concluded that the presented model is a first step into the implementation of a microstructural model into existing software simulations of the continuous casting process. Given that a greater amount of practical data were available, the validity of the model could be extended to an increasing number of steel grades or casting speeds. Moreover, experiments which focus on the determination of one special parameter, could increase the potential of the model. Nevertheless the model is a basis for future developments at the *CD-Laboratory for Metallurgical Fundamentals of Continuous Casting Processes* and will be expanded into different research projects.

Bibliography

[1] Wünnenberg, K.: Erstarrungsgefüge und Seigerungen in stranggegossenem Stahl. In: Metallurgie des Stranggießens, Verlag Stahleisen, Düsseldorf (1992).

[2] Michelic, S.: Thermal modelling of a continuous casting Machine. Proc. of the 12th International Students' Day of Metallurgy, Ostrava (2005), 61–69.

[3] Lechner, M.: Internal report. CD-Laboratory for Metallurgical Fundamentals of Continuous Casting Procceses (2005).

[4] Lechner, M.: Ph. D. Thesis in progress. University of Leoben (2006).

[5] Schwerdtfeger, K. (ed.): Metallurgie des Stranggießens. Verlag Stahleisen, Düsseldorf (1992).

[6] Lesoult, G., P. Neu and J.P. Birat: Modelling of equiaxed solidification induced by electromagnetic stirring on a steel continuous caster. Proc. of Metallurgical Applications of Magnetohydrodynamics, Cambridge (1982), 164–179.

[7] Ayata, K., T. Mori, T. Fujimoto, T. Ohnishi and I. Wakasugi: Improvement of macrosegregation in continuously cast bloom and billet by electromagnetic stirring. Transactions ISIJ, Vol. 24 (1984), 931–939.

[8] Fredriksson H. and A. Olsson: Mechanism of transition from columnar to equiaxed zone in ingots. Materials Science and Technology, Vol. 2 (1986), 508–516.

[9] Moore, J.J. and N.A. Shah: A review of the effects of electromagnetic stirring (EMS) in continuously cast steels – Part I. Iron & Steelmaker, Vol. 9 (1982), 31–36.

[10] Shah, N.A. and J.J. Moore: A Review of the effects of electromagnetic stirring (EMS) in continuously cast steels – Part II. Iron & Steelmaker, Vol. 9 (1982), 42–47.

[11] Kurz, W. and D.J. Fisher: Fundamentals of solidification. Trans. Tech. Publications, Aedermannsdorf (1989).

[12] Rauter, W.: Einfluss ausgewählter Gießparameter auf die Wärmeabfuhr in der Rundstranggießkokille. Diploma Thesis, University of Leoben (2001).

[13] Yao, M., H. Yin, J. Wang, D. Fang, Y. Liu, Y. Yu and J. Liu: Development of an experimental system for the study of the effects of electromagnetic stirring on mold heat transfer. Metallurgical and Materials Transactions B, Vol. 36B (2005), 475–478.

[14] Michelic, S.: Internal report. CD-Laboratory for Metallurgical Fundamentals of Continuous Casting Procceses (2006).

[15] Campanella, T. C. Charbon and M. Rappaz: Grain refinement induced by electromagnetic stirring: a dendrite fragmentation criterion. Metallurgical and Materials Transactions A, Vol. 35A (2004), 3201–3210.

[16] Hellawell, A., S. Liu and S.Z. Lu: Dendrite fragmentation and the effects of fluid flow in castings. Journal of Materials, (1997), 18–20.

[17] Hunt, J.D.: Steady state columar and equiaxed growth of dendrites and eutectic. Materials Science and Engineering, Vol. 65 (1984), 75–83.

[18] Thévoz, P., J.L. Desbiolles and M. Rappaz: Modeling of equiaxed microstructure formation in casting. Metallurgical and Materials Transactions A, Vol. 20A (1989), 311–322.

[19] Rappaz, M., C.A. Gandin, J.L. Desboiles and P. Thévoz: Prediction of grain structures in various solidification processes. Metallurgical and Materials Transactions A, Vol. 27A (1996), 695–705.

[20] Rappaz, M.: Modelling of microstructure formation on solidification processes. International Materials Reviews, Vol. 34 (1989), 93–123.

[21] Etienne, A.: Columnar and equiaxed dendrite growth in continuously cast products. Steel research, Vol. 61 (1990), 472–477.

[22] Gnauck, J.: Numerische Modellierung des Umschlags von gerichteter zu ungerichteter Erstarrung in Fe-C–Legierungen. Ph. D. Thesis, University of Berlin (2002).

[23] Lipton, J., W. Heinemann and W. Kurz: Columnar to equiaxed transition in castings – determination of the CET from cooling curves. Arch. Eisenhüttenwesenes, Vol. 55 (1984), 195–200.

[24] Thévoz P.: Modelling of columnar and equiaxed solidification, Internal Report Calcom SA.

[25] Lechner, M., J. Reiter, C. Bernhard, M. Forsthuber and O. Zach: Bestimmung und Bedeutung der Randbedingungen für die Simulation von Stranggießprozessen. BHM, Vol. 149 (2004), 101–106.

[26] Bernhard C., M. Lechner, E. Doringer, M. Forsthuber and W. Rauter: Numerical simulation of solidification in continuous casting of rounds. 5th International Metallurgical Conference on Continuous Casting of Billets and Modelling of the Steelmaking Process, Trinec (2003).

[27] Reiter, J.: Coherence of flow, casting parameters and crack sensitivity in a continuous casting mould. Diploma Thesis, University of Leoben (2004).

[28] Swaminathan, C. and V. Voller: A general enthalpy method for modeling solidification processes. Metallurgical Transactions B, Vol. 23B (1992), 651–664.

[29] Patankar, S.: Numerical heat transfer and fluid flow. Hemisphere Publishing Corporation (1980).

[30] Hunt, J.D. and S.Z. Lu: Numerical modeling of cellular/dendritic array gowth: spacing and structure predictions. Metallurgical Transactions A, Vol. 27A (1996), 611–623.

[31] Gäumann, M., R. Trivedi and W. Kurz: Nucleation ahead of the advancing interface in directional solidification. Materials Science and Engineering A, (1997), 763–769.

[32] Langer, J.S. and H. Muller-Krumbhaar: Stability effects in dendritic crystal growth. Journal of Crystal Growth, Vol. 42 (1977), 11–14.

[33] Mullins, W.W. and R.F. Sekerka, Journal of Applied Physics, Vol. 35 (1964), 444.

[34] Pilling J. and A. Hellawell: Communication: Mechanical deformation of dendrites by fluid flow. Metallurgical and Materials Transactions A, Vol. 27A (1996), 229–232.

[35] Harada, H., K. Miyazawa and T. Matsumiya: Numerical modeling of solidification structure formation under the molten steel flow. Proceedings of Modeling of Casting, Welding and Advanced Solidification X, (2003), 497–503.

[36] Dustin, I. and W. Kurz: Modeling of cooling curves and microstructures during equiaxed dendritic solidification. Zeitschrift für Metallkunde, Vol. 77 (1986), 265–273.

[37] Maxwell I. and A. Hellawell: Simple model for grain refinement during solidification, Acta Metall., Vol. 23 (1975), 229–237.

[38] Thévoz, P: Modelisation de la solidification dendritique equiaxe, Ph. D. Thesis, EPFL Lausanne (1988).

[39] Lipton, J., M.E. Glicksman and W. Kurz: Equiaxed dendrite growth in alloys at small supercooling. Metallurgical and Materials Transactions A, Vol. 18A (1987), 341–345.

[40] Maldovan, M., J. Príncipe, G. Sánchez, A. Pignotti and M. Goldschmit: Numerical modeling of continuous casting of rounds with electromagnetic stirring. European Congress on Computational Methods in Applied Sciences and Engineering, ECCOMAS 2000, Barcelona (2000).

[41] Das, S.K.: Mathematical simulation of the thermal field during continuous casting process by a nonorthogonal coordinate transformation formalism. Transactions of the Indian Institute of Metals, Vol. 47 (1994), 57–66.

[42] Spitzer, K.H: Berechnung von Strömungen beim elektromagntischen Rotationsrühren von Rundsträngen, Ph. D. Thesis, University of Clausthal (1985).

[43] Ludwig, A. and M. Wu: A three-phase model for mixed columnar-equiaxed solidification. Metallurgical and Materials Transactions A, Vol. 37A (2006), 1613–1631.

[44] Bernhard, C.: Mechanical properties and crack susceptibility of solidifying steels under continuous casting conditions, Ph. D. Thesis, University of Leoben (1998).

[45] Ayata, K., K. Narita, T. Mori and T. Ohnishi: Influence of electromagnetic stirring at mold on negative segregation in continuously cast bloom, Tetsu-to-Hagane, Vol. 67 (1981), 1278–1286.

A. Procedure Flowcharts

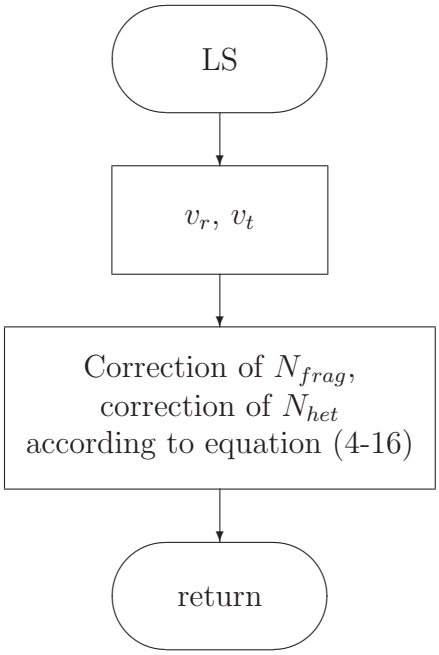

Figure A-1.: *Flowchart of computing transport at the inside curve of the strand.*

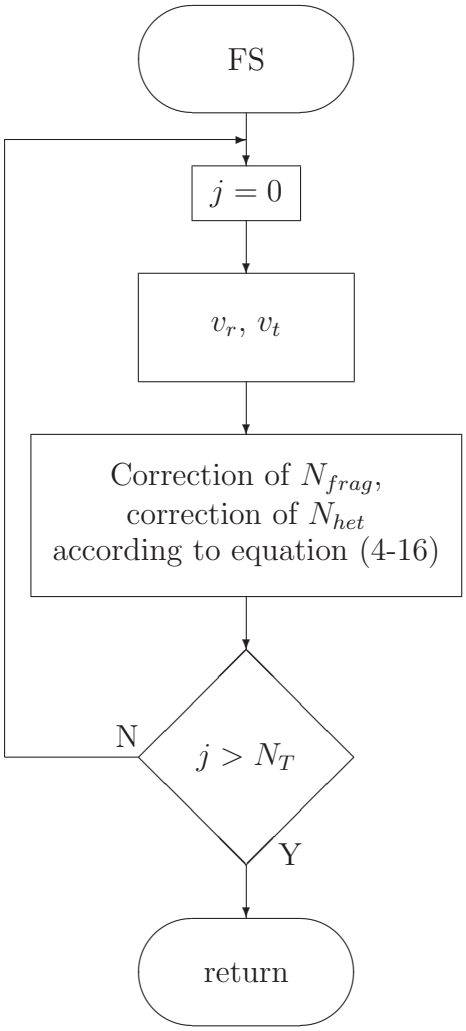

Figure A-2.: *Flowchart of computing transport at the outside curve of the strand.*

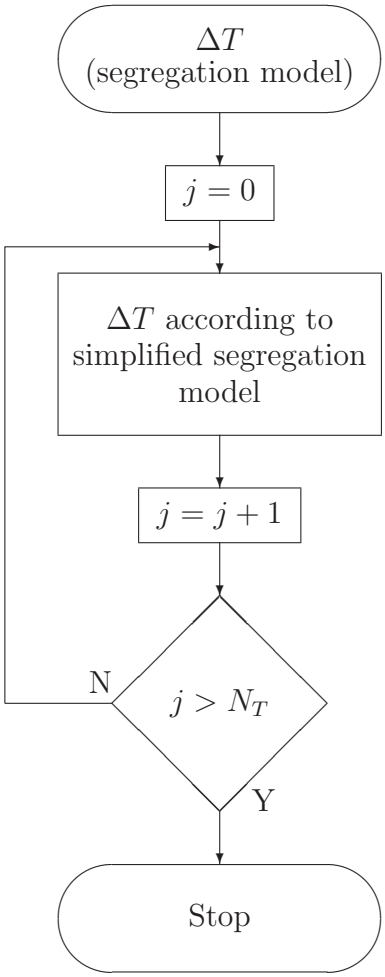

Figure A-3.: *Flowchart of computing the node undercooling.*

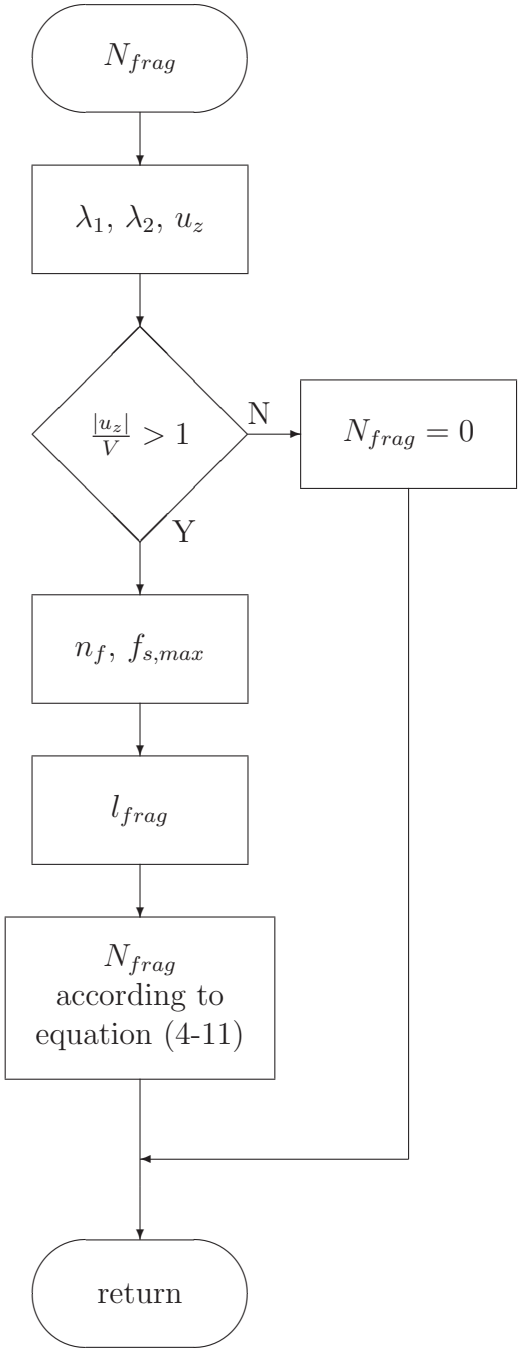

Figure A-4.: *Flowchart of computing the amount of fragmented dendrites* N_{frag}.

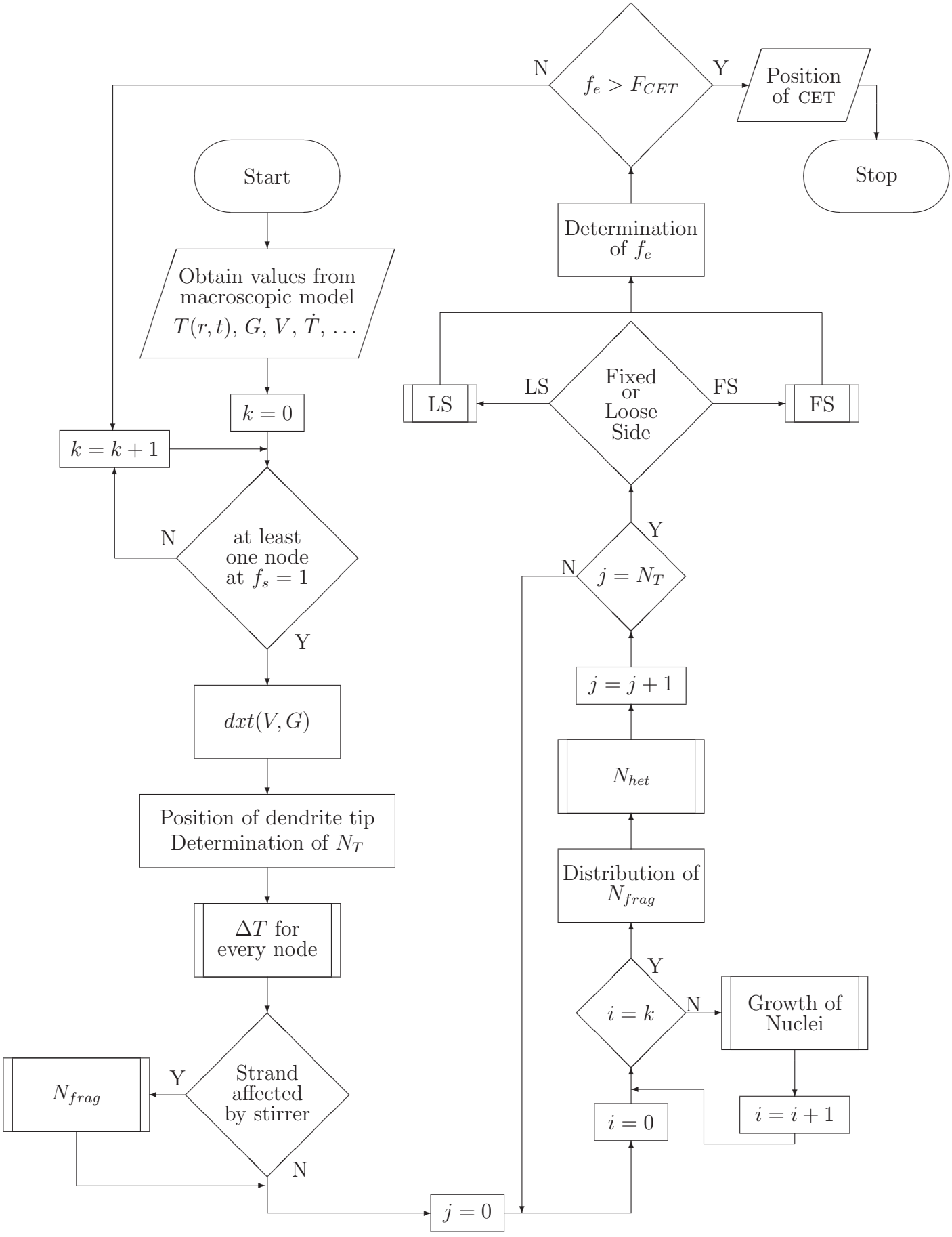

Figure A-5.: *Flowchart of microstructure model.*

B. Calculation of the Ivantsov function

The description of a dendrite tip similar to the one in **Fig. B-1** is best achieved by a paraboloid of revolution. Ivantsov [11] was the first to develop a mathematical analysis in 1947 – the corresponding function is since then termed IVANTSOV-function.

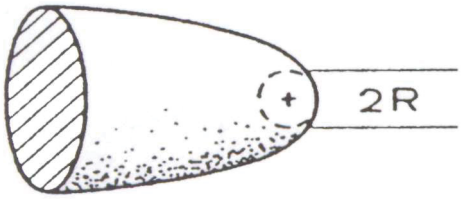

Figure B-1.: *A typical dendrite tip as the basis for* IVANTSOV*'s analysis. [11]*

According to Kurz and Fisher [11], it is given by

$$I(P) = P \cdot \exp(P) \cdot E_1(P) \tag{B-1}$$

where E_1 is the exponential integral function

$$E_1(P) = \int_P^\infty \frac{\exp(-z)}{z} \mathrm{d}z \tag{B-2}$$

which is best determined from the following series:

$$E_1(P) = -0.5772157 - \ln(P) - \sum_{i=1}^{\infty} \frac{(-1)^i \cdot P^i}{i \cdot i!} \tag{B-3}$$

The best numeric approach to the $I(P)$ for $1 \leq P \leq \infty$ is, according to [11],

$$I(P) = \frac{P^4 + a_1 P^3 + a_2 P^2 + a_3 P + a_4}{P^4 + b_1 P^3 + b_2 P^2 + b_3 P + b_4} \tag{B-4}$$

with

$a_1 = 8.5733287401$ $b_1 = 9.5733223454$

$a_2 = 18.059016973$ $b_2 = 25.632956148$

$a_3 = 8.6347608925$ $b_3 = 21.099653082$

$a_4 = 0.2677737343$ $b_4 = 3.9584969228$

For the case of $0 \leq P \leq 1$, E_1 is best approached by

$$E_1(P) = a_0 + a_1 P + a_2 P^2 + a_3 P^3 + a_4 P^4 - \ln(P) \tag{B-5}$$

with:

$a_0 = -0.57721566$ $a_1 = 0.99999193$

$a_2 = -0.24991055$ $a_3 = 0.05519968$

$a_4 = -0.00976004$ $a_5 = 0.00107857$

For quick estimates, it has been proven that $I(P)$ can also be approximated by a continued fraction of the type:

$$I(P) = \cfrac{P}{P + \cfrac{1}{1 + \cfrac{1}{P + \cfrac{2}{1 + \cfrac{2}{P + \ldots}}}}} \tag{B-6}$$

Lastly, equation **(B-6)** can, in be approximated by:

$$I(P) \cong P \tag{B-7}$$

C. Properties of the Steel Grade SB8X30N

Table C.I.: *Composition of the steel*

Alloying element	**Average amount**
C	0.815 %
Si	0.250 %
Mn	0.750 %
P	0.0100 %
S	0.0100 %
Cr	0.275 %
Mo	0.020 %
Ni	0.100 %
Al	0.010 %
Cu	0.100 %

Table C.II.: *Thermophysical properties at liquidus temperature*

Quantity	Value	
κ	34.89	$W\,m^{-1}\,K^{-1}$
ρ	7.012×10^6	$g\,m^{-3}$
c_p	0.801	$J\,g^{-1}\,K^{-1}$
L_H	237	$J\,g^{-1}$